

1 **Fine sediment in mixed sand-silt environments impact**
2 **bedform geometry by altering sediment mobility**

3 **S.I. de Lange¹, I. Niesten¹, S.H.J. van de Veen¹, J.H. Baas², J. Lammers¹, K.**
4 **Waldschläger¹, D. Boelee¹, A.J.F. Hoitink¹**

5 ¹Wageningen University, Department of Environmental Sciences, Hydrology and Environmental
6 Hydraulics, Wageningen, the Netherlands

7 ²School of Ocean Sciences, Bangor University, Menai Bridge, United Kingdom

8 **Key Points:**

- 9
- 10 • Adding finer, non-cohesive material to a sand bed increases the mobility of the
11 sand, resulting in an increased dune length.
 - 12 • Adding finer, weakly-cohesive silt to a sand bed, decreases the mobility of the sand,
13 which hampers dune formation and growth.
 - 14 • Sediment bed composition does not directly impact total hydraulic roughness, but
indirectly affects it via altering the bed morphology.

Corresponding author: Sjoukje de Lange, sjoukje.delange@wur.nl

Abstract

Geometric characteristics of subaqueous bedforms, such as height, length and leeside angle, are crucial for determining hydraulic form roughness and interpreting sedimentary records. Traditionally, bedform existence and geometry predictors are primarily based on uniform, cohesionless sediments. However, mixtures of sand, silt and clay are common in deltaic, estuarine, and lowland river environments, where bedforms are ubiquitous. Therefore, we investigate the impact of fine sand and silt in sand-silt mixtures on bedform geometry, based on laboratory experiments conducted in a recirculating flume. We systematically varied the content of sand and silt for different discharges, and utilized a UB-Lab 2C (a type of acoustic Doppler velocimeter) to measure flow velocity profiles. The final bed geometry was captured using a line laser scanner. Our findings reveal that the response of bedforms to an altered fine sediment percentage is ambiguous, and depends on, among others, bimodality-driven bed mobility and sediment cohesiveness. When fine, non-cohesive material (fine sand or coarse silt) is mixed with the base material (medium sand), the hiding-exposure effect comes into play, resulting in enhanced mobility of the coarser material and leading to an increase in dune height and length. However, the addition of weakly-cohesive fine silt reduces the mobility, suppressing dune height and length. Finally, in the transition from dunes to upper stage plane bed, the bed becomes unstable and bedform heights vary over time. The composition of the bed material does not significantly impact the hydraulic roughness, but mainly affects roughness via the bed morphology, especially the leeside angle.

Plain Language Summary

Underwater bedforms, such as dunes, are often found on the bed of rivers and deltas. These rhythmic undulations have specific shapes and sizes, and they affect how water flows. When the bed of the river is made up of sand, we can predict the dune height and length. However, mixtures of different-sized sediments are common in rivers, and it is unknown how this impacts the geometry of the dunes. Therefore, we did experiments in a flume, a laboratory facility to simulate a river, and we tested different sediment bed mixtures. We found that adding non-cohesive fine particles to the base material caused the base material to be more mobile, leading to longer dunes. However, when adding weakly-cohesive fine particles, the effect was the opposite, and the dunes became shorter due to the limited mobility of the sediment. Finally, we observed that under high flow conditions, the bed became unstable and different dune shapes occurred. We found that the friction the water experiences is not directly impacted by the sediment bed mixtures, but is mostly affected by the shape of the bedforms.

1 Introduction

River bedforms are ubiquitous in low-land rivers, and they are known to impact the river by altering its hydraulics, ecology, and sediment balance. The geometry of river bedforms, especially dunes, impacts the fairway depth (ASCE Task Force, 2002; Best, 2005), adds to the form roughness of the river bed (Warmink et al., 2013; Venditti and Bradley, 2022), and determines suitable foraging places for fish (Greene et al., 2020). It is therefore useful to predict the geometry of bedforms without having to perform regular field measurements. In non-supply limited conditions, river dunes may scale with flow depth (Allen, 1978). However, more recent studies have reinstated the observations by Yalin (1964), Van Rijn (1984), and Karim (1995), indicating a relation between bedform geometry and some measure of transport stage (Bradley and Venditti, 2019; Venditti and Bradley, 2022), where transport stage represents the ratio between flow strength and the mobility of the bed material. Dune length increases with transport stage, while dune height increases with transport stage until a maximum is reached, whereafter the height decreases and the bedforms start to wash out (Baas and Koning, 1995; Bradley and Venditti, 2019). This framework effectively predicts

dune height and length, despite considerable variability, which can be up to two-orders of magnitude (Bradley and Venditti, 2017). This variability may in part be attributed to the influence of bed composition on bedform geometry.

The bed composition, i.e. the grain size distribution of the bed sediment, is one of the primary determinants for bedform existence and size. Measures of grain size appear in almost all existing phase diagrams (Southard and Boguchwal, 1990; Berg and Gelder, 1993; Perillo et al., 2014), with the median grain size D_{50} as general parameterization. However, this simplification poses challenges when dealing with natural sediment mixtures characterized by complex, multimodal sediment size distributions, which are common in deltaic, estuarine and coastal environments featuring sediment mixtures of mud (i.e. clay and silt) and sand (Healy et al., 2002).

Recent research has focused on understanding how cohesive clay affects bedform geometry. It has been observed that even a small percentage of cohesive clay in sand-clay mixtures can effectively suppress bed mobility, resulting in a reduced bedform height (Schindler et al., 2015; Parsons et al., 2016) and limited bedform growth (Wu et al., 2022). It is, however, unknown what the impact of non- and weakly cohesive fine materials (silts and fine sands) is on dune morphology, despite their abundance in downriver environments.

A few studies explored the influence of silt on erodibility of the sediment bed. For instance, Bartzke et al. (2013) examined the behavior of sand ($300\ \mu\text{m}$)-silt ($50\ \mu\text{m}$) beds in an annular laboratory flume. They found that an increasing silt content, even at low percentages (as little as 0.18% silt), contributed to bed stabilization through a reduction in water inflow, attributed to pore-space plugging by silt. Yao et al. (2022) also reported increased stability (i.e., increased erosion threshold) with increasing silt content in their laboratory experiments, although stabilization only occurred at a silt content of $>35\%$, when a stable silt skeleton could be formed. Opposing Bartzke et al. (2013), a change in bed stability was not observed at lower silt contents.

Additionally, Ma et al. (2017) and Ma et al. (2020) studied a silt-rich sediment bed ($D_{50} = 15 - 150\ \mu\text{m}$) with low dunes in the Yellow River. Ma et al. (2020) showed that the presence of fine sediment (silt) led to a shift from a low-efficiency sediment transport regime (following the Engelund-Hansen equations (Engelund and Hansen, 1967)) to a high-efficiency regime. The high-efficiency regime prevailed for sediment beds with a medium grain size smaller than $88\ \mu\text{m}$, and, in the transitional range ($88\ \mu\text{m} < D_{50} < 153\ \mu\text{m}$), the existence of this regime depended on sorting of the material ($\sqrt{D_{84}/D_{16}}$). They argued that the shift from a low- to a high-efficiency transport regime resulted from the transition from mixed load to suspended sediment transport, caused by the presence of silt.

Yet, none of these studies discussed the potential impact of silt content on bedforms. This is an important research gap, because an increase in bed stability, as observed by Bartzke et al. (2013) and Yao et al. (2022), could theoretically reduce bedform formation and growth due to a decrease in sediment transport, whilst Ma et al. (2020)'s suspension-load dominated high-efficiency regime would also mean suppression of bedform formation and growth, but then because bedload transport gets increasingly replaced by suspended load transport, which is incapable of forming bedforms. Clearly, the effect of silt in sand-silt mixtures on the resulting bedform geometry is largely unexplored. Therefore, our research seeks to address the following question: What is the influence of the fraction non-cohesive and weakly cohesive fine sediment in sand-silt mixtures on the dynamic equilibrium bedform geometry and the resulting hydraulic roughness?

To answer this question, we conducted 52 laboratory experiments in a recirculating flume, in which the influence of fine sand and silt percentage in sand-silt mixtures on bedform geometry was studied. For three flow velocities, three different sediment mixtures, largely falling within the studied range of Ma et al. (2020), were tested by systematically mixing various fractions of fine sand, coarse silt and fine silt with a coarser base material of

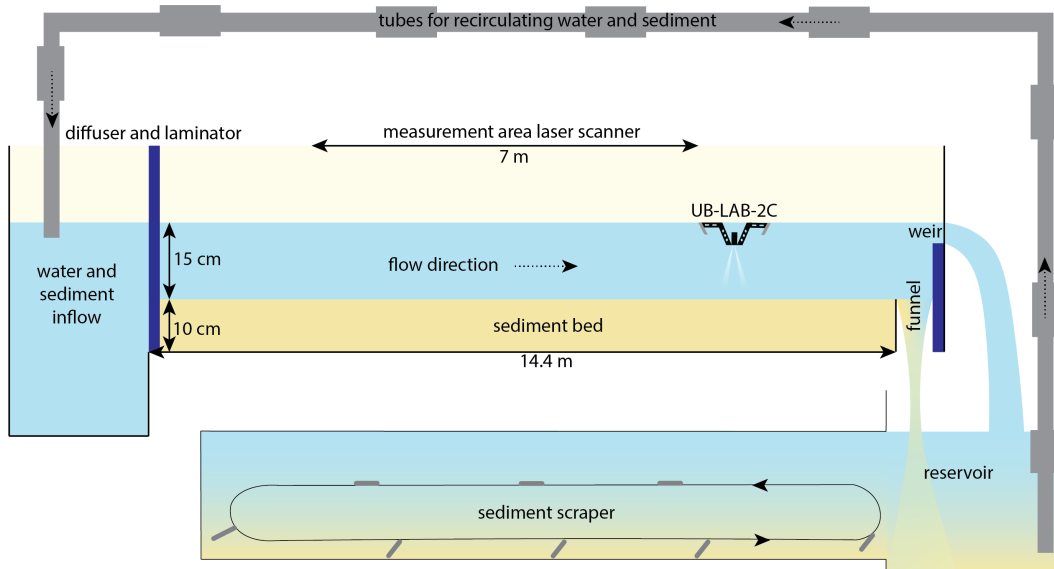


Figure 1. Schematic drawing of the experimental setup. The flume recirculates both water and sediment.

116 medium sand. These experiments allowed us to assess how different sizes of fine sediment
 117 in a sand-silt mixture affect the transport stage and the resulting bedform geometry under
 118 different flow conditions. In the following sections, we provide a detailed description of the
 119 experimental setup, after which we discuss the different equilibrium bedform geometries
 120 that resulted from the experiments. We argue that the hiding-exposure effect enhances the
 121 mobility of the coarser fraction, whereas cohesion from fine silt decreases the bed mobility,
 122 leading to deviations from the expected relationship between transport stage and bedform
 123 dimensions.

124 2 Methods

125 2.1 Experimental setup

126 The experiments were conducted in a tilting flume with recirculation facilities for both
 127 water and sediment in the Kraijenhoff van de Leur Laboratory for Water and Sediment
 128 Dynamics of Wageningen University and Research (Figure 1 and 2). The flume has an
 129 internal width of 1.20 m, a length of 14.4 m, and a height of 0.5 m. The water level is
 130 controlled by adjusting a downstream weir. A diffuser (Figure 2a) at the upstream part
 131 ensures that the inflow is distributed over the entire width of the flume. The diffuser is
 132 followed by a stacked pile of PVC tubes that serve as a laminator, suppressing turbulence
 133 at the inflow section. At the end of the flume, a funnel was installed to channel bedload
 134 material to a lower reservoir (Figure 1), and to prevent deposition in front of the weir. A
 135 continuously running sediment scraper ensures that the sediment stays in suspension in the
 136 lower reservoir, upon being pumped back to the inflow of the flume. At the end of one
 137 experiment (35% fine sand, medium discharge) the sediment funnel was clogged and the
 138 sediment was not fully recirculated. This run was excluded from the analysis.

139 The flow depth was set to 15 cm, measured from the initial flat sediment bed, and it was
 140 kept the same for all experimental runs by adjusting the weir height. The slope was set
 141 to 0.01 m m^{-1} . Experimental runs were performed for different discharges (low: 45 L s^{-1} ;
 142 medium: 80 L s^{-1} ; high: 100 L s^{-1}), to be able to distinguish the effects of different trans-

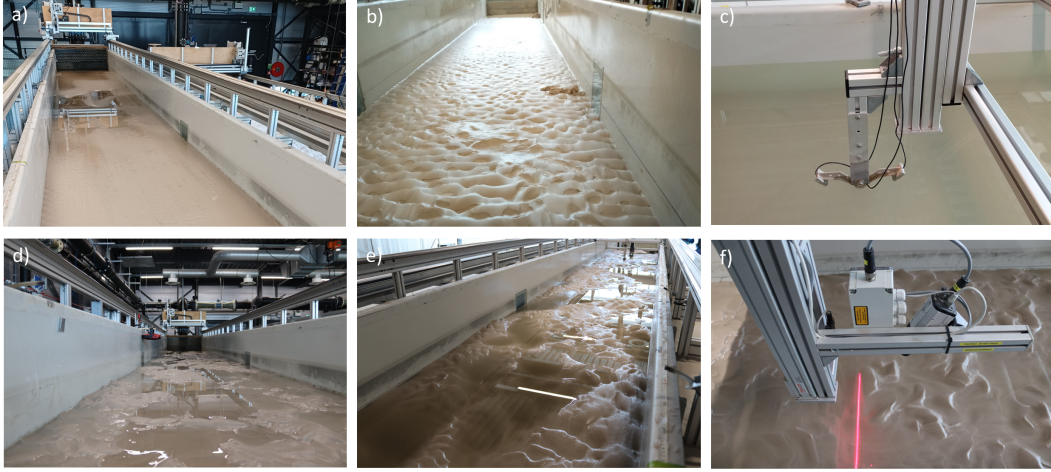


Figure 2. Pictures of the laboratory flume and the instrumentation. a) Flume with flatbed, facing upstream, including the upstream-located diffuser. b) Bed covered with small bedforms, facing downstream, including the downstream-located weir. c) UB-Lab 2C flow velocity profiler. d) Dune-covered bed, facing upstream. e) Dune-covered bed, facing downstream, with the UB-Lab 2C in background. f) Line laser scanner.

143 port stages on bedform morphology. The discharge was monitored and regulated with an
 144 electromagnetic flow meter. The corresponding calculated width- and depth-averaged flow
 145 velocities were 0.25, 0.44 and 0.56 m s⁻¹, the corresponding depth-averaged flow velocities
 146 in the middle of the flume (measured with an UB-Lab 2C, see section 2.2) were slightly
 147 larger due to a side-wall effect (0.30, 0.45 and 0.58 m s⁻¹, respectively). The experiments
 148 were run for 12, 5 and 3 hours for the low, medium, and high discharges, respectively. Based
 149 on the ripple size predictor of Soulsby et al. (2012), the medium-sand ripples formed in the
 150 low-discharge experiments reached about 80% of their equilibrium height and length after
 151 12 hours. Their planform at this development stage was linguoid, which agrees with the
 152 planform predicted by ripple development model of Baas (1999). Naqshband et al. (2016)
 153 studied the dune equilibrium time for medium sand (290 μm). Their equilibrium dimen-
 154 sions were reached after 3 hours for the experiments with a flow velocity of 0.64 m s⁻¹ and
 155 after 1.5 hours for 0.80 m s⁻¹. This suggests that the dunes formed at medium and high
 156 discharges in the present experiments reached equilibrium size.

157 The flow was sub-critical and turbulent during all experiments, determined by the
 158 Froude number, Fr (-), being smaller than 1 (0.30, 0.54 and 0.69, respectively) and the
 159 Reynolds number, Re (-), being larger than 4000 (38000, 67000, 83000, respectively), calcu-
 160 lated with:

$$Fr = \frac{u}{\sqrt{gh}} \quad (1)$$

$$Re = \frac{hu}{\nu} \quad (2)$$

161 where u is the time and depth-averaged flow velocity (m s⁻¹), g is the gravitational
 162 acceleration (9.81 m s⁻²), h is the water depth (0.15 m), and ν is the kinematic viscosity
 163 (m² s⁻¹), which is weakly dependent on water temperature, t (°C), as $\nu = 4 * 10^{-5} / (20 + t)$.
 164 Here, $\nu = 1.05 * 10^{-6}$ m² s⁻¹ for 18 °C is used.

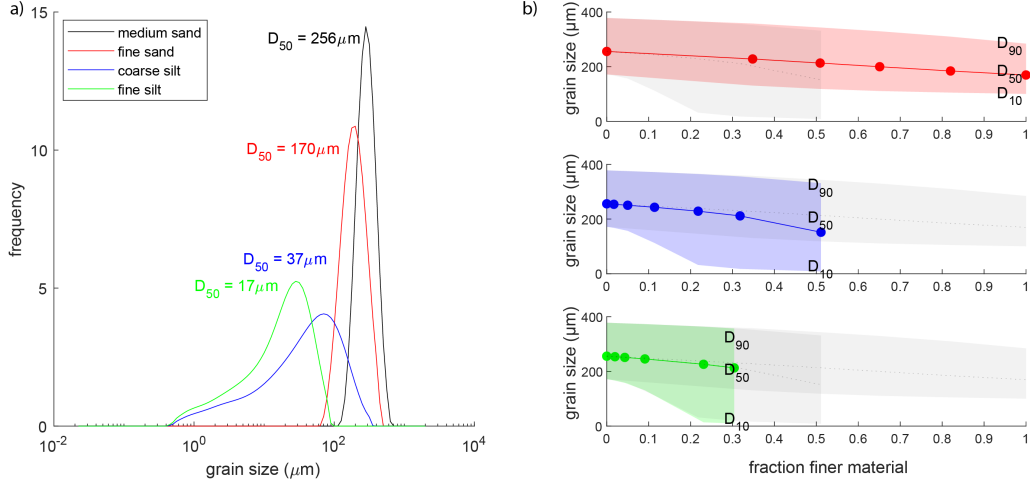


Figure 3. a) Grain-size distributions of the sediments used in the experiments. b) D_{10} , D_{50} and D_{90} of the tested mixtures, in which the finer material (fine sand, coarse silt or fine silt) is mixed with the base material (medium sand).

165 A sediment bed with a thickness of 0.10 m was applied, which consisted of a mixture of
 166 two grain sizes: a base sediment of medium sand (median size, $D_{50} = 256 \mu\text{m}$), mixed with
 167 fine sand ($D_{50} = 170 \mu\text{m}$), coarse silt ($D_{50} = 37 \mu\text{m}$) or fine silt ($D_{50} = 17 \mu\text{m}$) (Figure 3a
 168 and Supplementary Figure S1 for images of the sediment). All sediments were composed of
 169 silica (SiO_2). The particle size distribution of the original sediments was measured with a
 170 Mastersizer 3000 (Figure 3). The fine sand and coarse silt are non-cohesive, whereas the fine
 171 silt could be classified as weakly-cohesive (Wolanski, 2007), confirmed by visual observation
 172 of the sticky fine silt slurry and a significantly higher submerged angle of repose (40° instead
 173 of 30° for sand). No visible flocculation of the silt fraction occurred during the experiments.

174 The weight percentage of finer material mixed with the base material ranged from 0 to
 175 100 wt% for fine sand, to 51 wt% for coarse silt (with 49 wt% medium sand) and to 30 wt%
 176 for fine silt (with 70 wt% medium sand). In total, 17 different mixtures were tested, which
 177 were all exposed to the low, medium and high discharge. In Table 1, an overview of the
 178 experimental mixtures is given. The D_{50} and 90th-percentile, D_{90} , values of the mixtures
 179 hardly changed when adding finer material, but the 10th-percentile, D_{10} , values dropped
 180 significantly when adding coarse or fine silt (Figure 3b).

181 2.2 Instrumentation

182 A line laser and 3D camera (Figure 2f), equipped with Gigabit Ethernet (SICK, 2012),
 183 was used to scan the bed topography. The devices were mounted on a measurement carriage
 184 that moved on fixed rails along the flume. After every experimental run, the flume was slowly
 185 drained, and an area of 7 x 1 m was recorded in three parallel, partially overlapping, swaths,
 186 with a resolution of 0.1 mm. See Ruijsscher et al. (2018) for a detailed description of the
 187 line laser scanner.

188 During the first and last 30 minutes of an experimental run, an UB-Lab 2C (UBER-
 189 TONE) (Figure 2c) was deployed to measure flow velocity profiles. The UB-Lab 2C is an
 190 ADVP (acoustic Doppler velocity profiler, e.g. Hurther and Lemmin (2001) and Mignot et
 191 al. (2009)), which measures a two-component velocity profile at high spatial (1.5 mm) and
 192 temporal resolution, here 10 to 15 Hz. An acoustic signal is transmitted along a single beam
 193 and received by two receivers under different observation angles. The resulting 2-component

Table 1. Overview of the performed experiments. Seventeen different sediment mixtures were tested, in which the type and percentage of fine material relative to the coarse material (base material) varied per experimental run. Each experiment with a distinct mixture was conducted for low, medium and high discharge, resulting in 51 experiments. * the experiment with medium discharge was excluded from analysis because of clogging of the pumps.

experiment number	% fine / % coarse
<i>base experiment</i>	
1	0/100
<i>experiments with fine sand</i>	
2-4	35/65*
5-7	51/49
8-10	65/35
11-13	82/18
15-18	100/0
<i>experiments with coarse silt</i>	
19-21	2/98
22-24	5/95
25-27	11/89
28-30	22/78
31-33	32/68
34-36	51/49
<i>experiments with fine silt</i>	
37-39	2/98
40-42	4/96
43-45	9/91
46-48	23/77
49-51	30/70

194 vector is then projected to yield the 2-dimensional velocity in the streamwise direction (u)
 195 and vertical direction (w) along the beam (1D-profile). The emission frequency was set to
 196 1 MHz with a bin size of 1.5 mm. The pulse repetition frequency ranged from 1200 to 1800
 197 Hz for low and high discharge, respectively.

198 2.3 Data analysis

199 2.3.1 Sediment characterization

200 The behavior of the sediment in the experiments was estimated from the span value of
 201 the sediment-size distribution and the dominant way of sediment transport. This informa-
 202 tion was later used to interpret the observed bedform patterns.

203 The span value of the tested mixtures was used as a measure of distribution width, and
 204 was defined as:

$$SV = \frac{D_{90} - D_{10}}{D_{50}} \quad (3)$$

205 The sorting was determined as:

$$\sigma_g = \sqrt{\frac{D_{84}}{D_{16}}} \quad (4)$$

206 To determine the dominant way of transport, the ratio between the settling velocity of
 207 a particle, w_s , and the shear velocity, u^* , was calculated. If this ratio is larger than 3, the
 208 dominant transport mode is expected to be bedload, and if the ratio is smaller than 0.3,
 209 the dominant mode is expected to be suspended load (Dade and Friend, 1998). In between
 210 these values, the transport mode is mixed.

211 The settling velocity of a particle was approximated with (Ferguson and Church, 2004;
 212 Dietrich, 1982):

$$w_s = \frac{\rho_r g D_{50}^2}{C_1 \nu + \sqrt{0.75 C_2 R g D_{50}^3}} \quad (5)$$

213 where ρ_r is the relative submerged density = $(\rho_s - \rho_w)/\rho_w$, and $C_1 = 18$ and $C_2 = 1$
 214 for natural grains (Ferguson and Church, 2004). The D_{50} of the original sediments was used
 215 rather than the D_{50} of the mixture, giving a transport mode for the base sediment and the
 216 finer fraction separately. This approximation was verified by visual observation through a
 217 window in the side of the flume.

218 2.3.2 Bedform geometry

219 Final bed configurations were determined from the bed elevation data obtained with
 220 the line laser scanner. Five longitudinal transects were constructed across the width of
 221 the flume, with an interspacing of 200 mm. The resulting transects served as input for
 222 the bedform tracking tool of Mark and Blom (2007), which gives bedform geometry based
 223 on specific detrending lengths, used to differentiate between bedform scales. Two bedform
 224 length scales were identified: 150 ± 100 mm (hereafter referred to as small bedforms), and
 225 1100 ± 400 mm (referred to as large bedforms). Small bedforms were observed in the
 226 low-discharge experiments, whilst larger bedforms were observed in the medium and high-
 227 discharge experiments, and the bedform tracking tool was applied accordingly. Only if the
 228 bedform occurred in at least two profiles of a bed scan, bedform statistics were calculated.

229 Bedform characteristics (Figure 4) in this study included bedform height, Δ (m), the
 230 vertical distance between crest and downstream trough; bedform length, λ (m), the horizon-

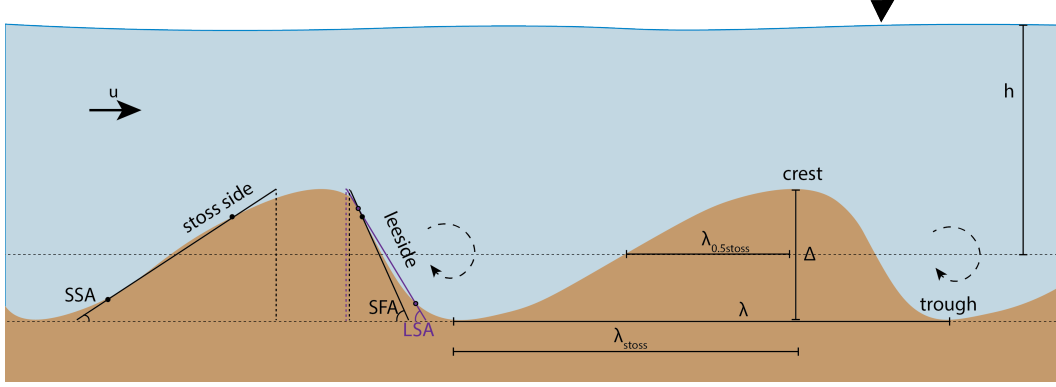


Figure 4. Definition of the bedform characteristics, showing the bedform height (Δ), the length (λ), the total length of the stoss side (λ_{stoss}) and the length of the stoss side at $0.5*\Delta$ ($\lambda_{0.5stoss}$), the leeside angle (LSA), in which the upper and lower 1/6th of the leeside is excluded, the stoss-side angle (SSA), also excluding the upper and lower 1/6th of the stoss side, and the slip-face angle (SFA), which is the steepest part (95-percentile) of the leeside. The steepest part of the leeside is indicated with a small purple marker, and the location of the upper and lower 1/6th of the lee and stoss side are indicated with a small black marker.

231 tal distance between two subsequent crests; leeside angle, LSA ($^\circ$), the slope angle derived
 232 from a linear fit of the bedform's leeside, excluding the upper and lower 1/6 of the bed-
 233 form height; stoss-side angle, SSA ($^\circ$), calculated similarly to the leeside angle; and the
 234 slip-face angle, SFA ($^\circ$), the steepest part of the leeside, calculated as the 95-percentile of
 235 the distribution of angles along the leeside. The bedform roundness index, BRI , of the small
 236 bedforms was defined as the ratio between the length from the dune crest to the stoss side at
 237 0.5 times the dune height ($\lambda_{0.5stoss}$) and the length of the stoss side (λ_{stoss}) (Perillo et al.,
 238 2014; Prokocki et al., 2022). A bedform was classified as rounded if $BRI \geq 0.6$. Finally, the
 239 bedform width, W (m), was derived by constructing six cross-sectional profiles transverse
 240 to the flow, with an interspacing of 1000 mm. Next, the same bedform tracking tool was
 241 applied using the same settings as for the longitudinal profiles. The bedform width was
 242 calculated only for the low-discharge experiments, where the width of the bedforms was
 243 considerably smaller than the width of the flume.

244 2.3.3 Bedform geometry predictors

245 Various bedform geometry predictors were tested based on our data. The selected
 246 predictors for dune height and length included a measure of flow strength (Van Rijn, 1984;
 247 Venditti and Bradley, 2022), and the predictor of Soulsby et al. (2012) was used for the
 248 height and length of ripples.

249 Van Rijn (1984) developed an empirical dune height and length predictor, the former
 250 being dependent on the transport stage, T_{vRijn} , as measure of flow strength.

$$\Delta_{vRijn} = 0.11h \left(\frac{D_{50}}{h} \right)^{0.3} (1 - e^{-0.5T_{vRijn}})(25 - T_{vRijn}) \quad (6)$$

$$\lambda_{vRijn} = 7.3h \quad (7)$$

251 T_{vRijn} depends on shear stress and critical shear stress. See Appendix A for a full
 252 explanation.

253 Venditti and Bradley (2022) developed an empirical equation based on a different trans-
 254 port stage, T_{VB} , defined as $\frac{\theta}{\theta_c}$, which is the ratio of the dimensionless shear stress, θ , and
 255 critical shear stress, θ_c . The equations suitable for laboratory flows with a water depth less
 256 than 0.25 m are:

$$\Delta_{VB} = h \left(-0.00100 \left(\frac{\theta}{\theta_c} - 17.7 \right)^2 + 0.417 \right) \quad (8)$$

$$\lambda_{VB} = h \left(0.0192 \left(\frac{\theta}{\theta_c} - 8.46 \right)^2 + 6.23 \right) \quad (9)$$

257 The geometry of ripples is only dependent on a measure of grain size (D^*) and inde-
 258 pendent of transport stage (Baas, 1994; Baas, 1999). According to the equations of Soulsby
 259 et al. (2012), their geometry can be predicted with:

$$\Delta_{Soulsby} = D_{50} 202 D^{*-0.554} \quad (10)$$

$$\lambda_{Soulsby} = D_{50} (500 + 1881 D^{*-1.5}) \quad (11)$$

260 All definitions and symbols are given in Appendix A.

261 **2.3.4 Roughness characterization**

262 Hydraulic roughness was estimated following two methods. Firstly, the measured veloc-
 263 ity profiles were used, following the method of Hoitink et al. (2009). Secondly, an indirect
 264 hydraulic roughness predictor of Van Rijn (1984) was used, based on bed geometry and
 265 sediment characteristics.

266 The first method is based on the Law of the Wall:

$$\frac{\bar{u}(z)}{u^*} = \frac{1}{\kappa} \ln \left(\frac{z+h}{z_0} \right) \quad (12)$$

267 where \bar{u} is the mean velocity (m s^{-1}), $\kappa = 0.4$ is the Von Karman constant, h is the
 268 mean water depth (m), z is the height above the bed (m), and z_0 is roughness length (m).

269 For a water column that satisfies equation (12), i.e. where the velocity profiles are
 270 logarithmic (Supplementary Figure S3), the shear velocity can be determined from the slope
 271 of the velocity versus dimensionless depth σ_d (equation (B2)). This, in turn, can be used
 272 to derive roughness length and, ultimately, Manning's n, n_{man} ($\text{s m}^{-1/3}$). See Appendix B
 273 for an elaborate definition. Experiments 13-18 were excluded from analysis, since erroneous
 274 mounting caused invalid profiles.

275 Roughness was also approximated indirectly based on the predictor of Van Rijn (1984).
 276 The total predicted hydraulic roughness, expressed as friction factor, \hat{f} , results from form
 277 friction and grain friction (Einstein, 1950). The total hydraulic roughness was predicted as
 278 in Van Rijn (1984):

$$\hat{f} = \frac{8g}{(18 \log(\frac{12h}{k_s}))^2} \quad (13)$$

279 where k_s is a measure of roughness both consisting of form roughness and grain rough-
 280 ness. See Appendix B for the corresponding equations.

281 Friction factor \hat{f} can be converted to n_{man} via (Manning, 1891; Silberman et al., 1963):

$$n_{man} = \frac{R_h^{1/6}}{\sqrt{\frac{8g}{f}}} \quad (14)$$

282 where R_h is the hydraulic radius, which is equal to the cross-sectional area (A) divided
 283 by the wetted perimeter ($P = \text{width} + 2h$).

284 **3 Results**

285 **3.1 Observed bed geometries**

286 The bed geometries in the experiments were dependent on discharge (Figure 5a-c, see
 287 Supplementary Figures S2-S4 for the bed geometry of all runs), and on the addition of fine
 288 material. Below, we show the results separately for low, medium and high discharge.

289 **3.1.1 Low discharge bed geometries**

290 At low discharge, only small bedforms appeared on the bed (Figure 5a). The small
 291 bedforms had an average height of 0.011 m, an average length of 0.12 m and a non-rounded
 292 shape with a slip-face angle of 22°.

293 Bedform height and width both decreased with the addition of coarse silt and fine silt,
 294 which is especially pronounced at a silt percentage above 20% (Figure 6a). The bedform
 295 height decreased by 38% for coarse silt and 28% for fine silt compared to the experiment with
 296 pure medium sand. The corresponding decrease in length was considerably smaller (14%
 297 and 4%, respectively). This decrease in bedform height was not visible in the experiments
 298 with fine sand. Similarly, bedform width decreased by 11% and 23% for coarse and fine silt
 299 (Figure 6c), indicating that the bedforms became more three-dimensional in shape. The
 300 *LSA*, *SFA* and *BRI* of these bedforms were independent of the type and percentage of finer
 301 material added (Figure 6d-f).

302 **3.1.2 Medium discharge bed geometries**

303 The bedforms generated during medium discharge were generally larger than those
 304 that emerged during low discharge, with an average height of 0.027 m, a length of 0.54 m,
 305 and a slightly lower slip-face angle of 20°. Those bedforms followed two general trends.
 306 Firstly, the runs with an increasing amount of fine sand and coarse silt showed an increase
 307 in bedform height and length (Figure 5b). Especially for the coarse-silt runs, the increase
 308 in bedform length was considerable (Figure 7b). The bedform length in these runs was on
 309 average 0.59 m for the experiments with 20% coarse silt or less, and increased to 1.1 m for
 310 the experiments with a higher coarse-silt percentage in the bed. This increase in bedform
 311 length was accompanied by a smaller increase in bedform height from 0.032 m to 0.043 m
 312 (Figure 7a). Bedform heights and lengths for the experiments with fine sand were smaller
 313 than for the experiments with coarse silt (on average $\Delta = 0.026$ m and $\lambda = 0.54$ m for fine
 314 sand, and $\Delta = 0.035$ m and $\lambda = 0.73$ m for coarse silt). The lee-face angles varied per
 315 experiment, but the slip-face angles remained relatively constant, lacking a consistent trend
 316 with increasing content of fine material (Figure 7c and d).

317 The experiments with fine silt revealed smaller bedforms that were larger than the
 318 bedforms in the low-discharge experiments, but comparable in planform (Figure 5d), despite
 319 the clear increase in depth-averaged flow velocity. The mean bedform length was 0.38
 320 m, which is significantly smaller than for the experiments with fine sand and coarse silt.
 321 However, at 0.025 m, the mean bedform height is comparable to the runs with fine sand. A
 322 decrease in length and height was observed for the runs with 0 to 30% fine silt (23% decrease

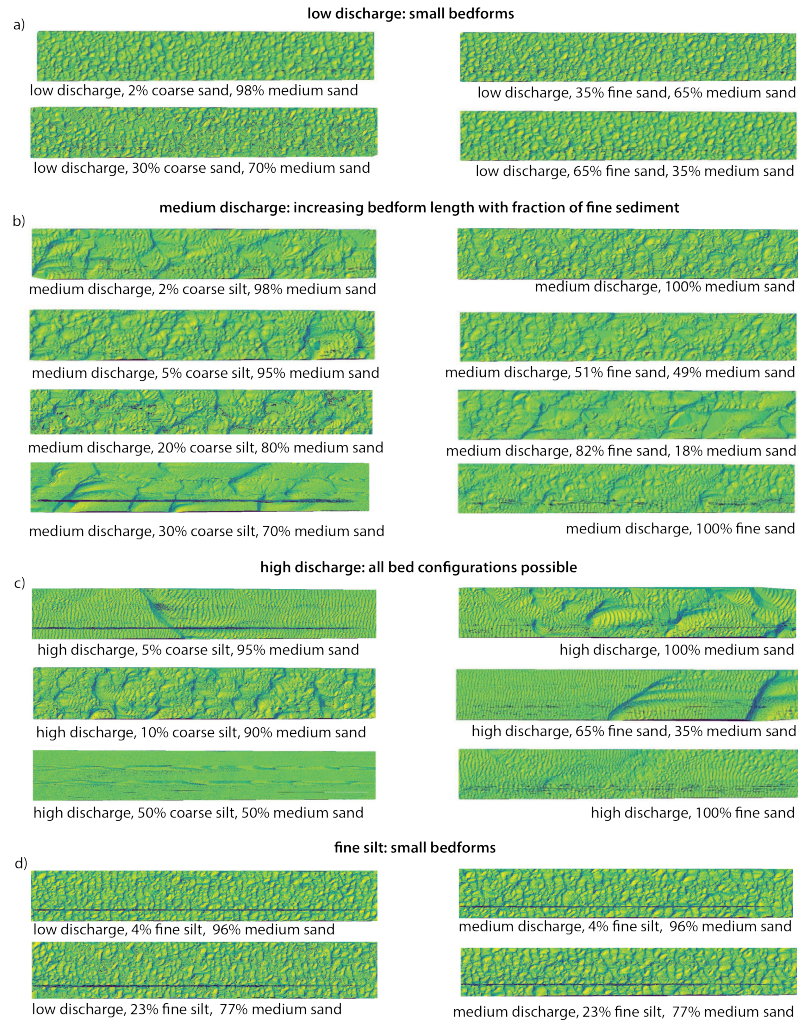


Figure 5. Dynamic equilibrium bed morphologies at the end of selected experiments. All images represent a 1 m wide and 7 m long section of flume. a) Bed morphologies at low discharge. b) Bed morphologies at medium discharge, showing increasing dune length with increasing finer material. c) Bed morphologies with large variability at high discharge. d) Impact of fine silt on bed morphology. Scans in (c) show small two-dimensional ripples superimposed on larger bedforms and flat beds. These ripples are artifacts caused by draining the flume over an almost flat bed (see Supplementary Figure S5 for verification).

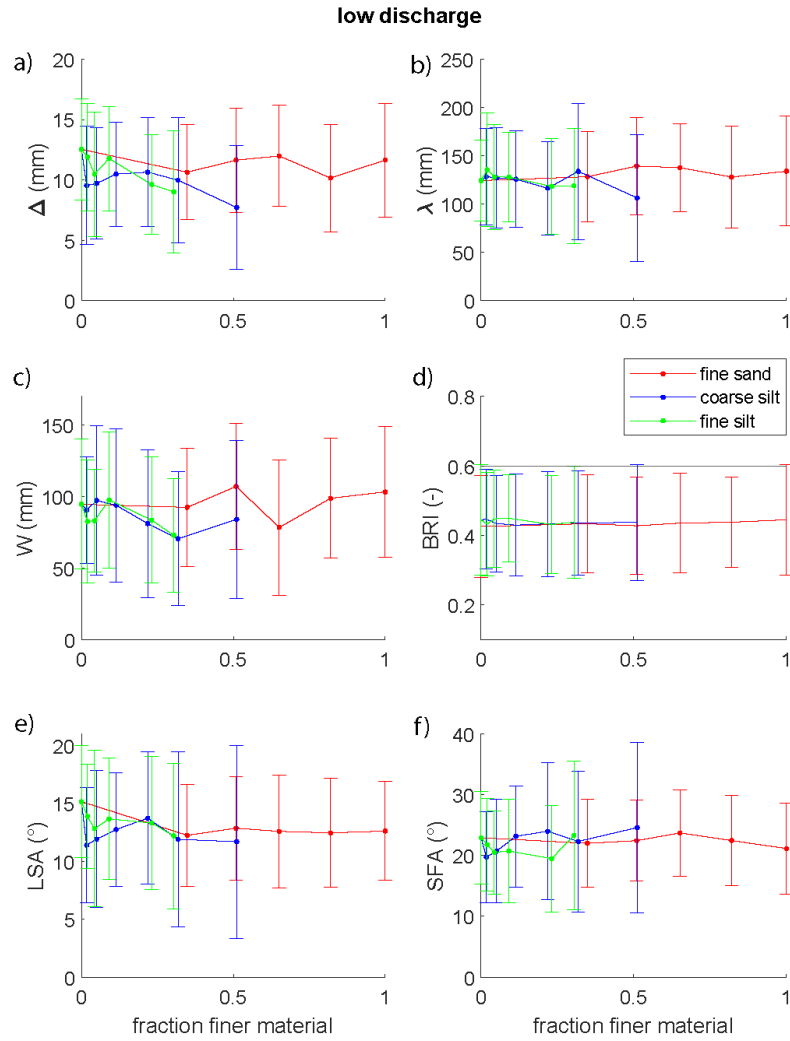


Figure 6. Bedform geometries at low discharge (45 L s^{-1}). a) Bedform height, Δ . b) Bedform length, λ . c) Bedform width, W . d) Bedform roundness index, BRI , where $BRI < 0.6$ indicates non-rounded bedforms. e) Leeside angle, LSA . f) Slip-face angle, SFA .

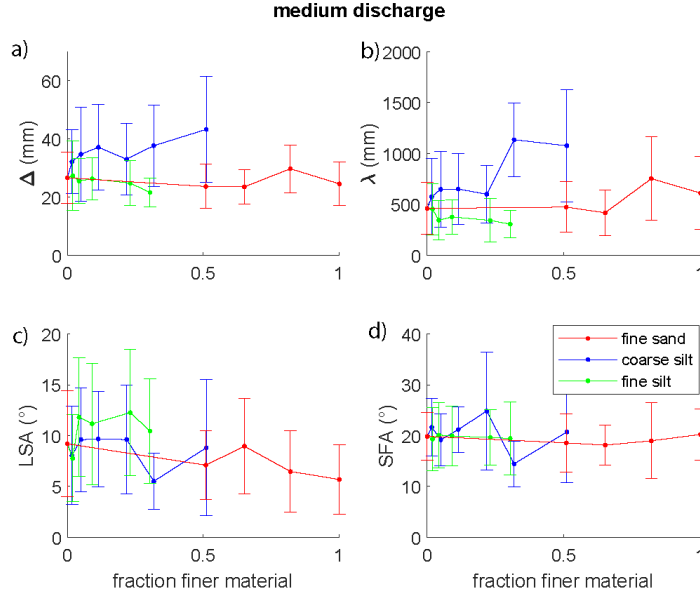


Figure 7. Bedform geometries at medium discharge (80 L s^{-1}). a) Bedform height, Δ . b) Bedform length, λ . c) Leaside angle, LSA . d) Slip-face angle, SFA .

323 in bedform height, 51% decrease in bedform length). Leaside angles were 28% larger than
 324 in the experiments with fine sand and coarse silt, but the slip-face angles were comparable.

325 **3.1.3 High discharge bed geometries**

326 The bedforms formed at high discharge were on average slightly larger than during
 327 medium discharge (Figure 8), with an average height of 0.029 m and length of 0.72 m.
 328 The slip-face angle was 18° , which was slightly lower than at medium discharge. However,
 329 the geometrical parameters were highly variable, with a standard deviation of 1.6 cm, 39
 330 cm, 4.6° for bedform height, length and slip-face angle, respectively, and without a clear
 331 relationship with the amount of fine material. The experiments with fine silt resulted on
 332 average shorter bedform lengths and higher leaside angles than the experiments with coarse
 333 silt and fine sand, which agrees with the observations at medium discharge.

334 The high discharge experiments were conducted close to the suspension threshold (w_s
 335 / $u^* < 0.3$), and the bedforms started to wash out towards upper stage plane bed, when
 336 three alternating bed states were observed (Figure 5c): an almost flat bed with one or two
 337 large, steep bedforms; a bed covered with dunes; and a flat bed.

338 **3.2 Bedform variability**

339 Relationships between bedform geometry and transport stage, θ/θ_c , are evident from
 340 the experimental data. Bedform length increased, and leaside and slip-face angle decreased
 341 with increasing transport stage, whereas the relationship between bedform height and trans-
 342 port stage approached a parabola (Figure 9a-d). Additionally, the variability in bedform
 343 geometry increased with increasing transport stage, indicated by the gray shaded band in
 344 Figure 9a-d.

345 The near-bed velocity $U_{0.2}$, which is the time-averaged velocity at the dimensionless
 346 height above the bed of $\sigma_d = 0.2$ and directly measured with the UB-Lab 2C, is a repre-

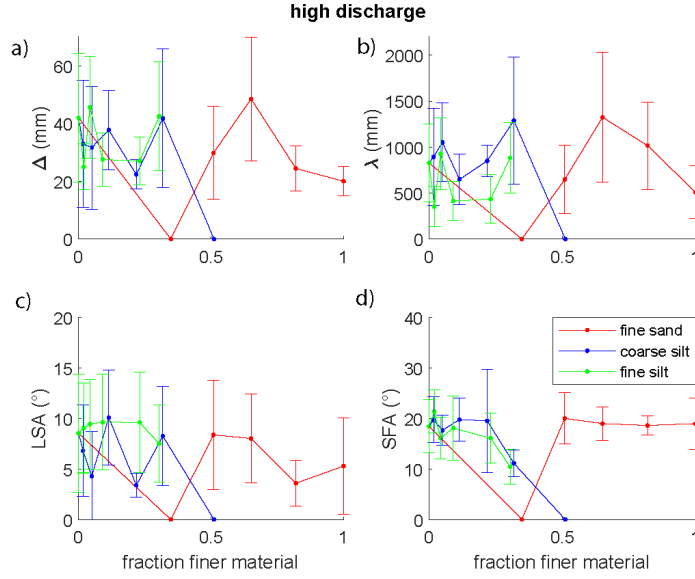


Figure 8. Bedform geometries at high discharge (100 L s^{-1}). a) Bedform height, Δ . b) Bedform length, λ . c) Leeside angle, LSA. d) Slip-face angle, SFA. Zero values indicate a flat bed.

347 presentation of the near-bed conditions influencing and being influenced by the bed geometry.
 348 The near-bed velocity shows a strong relation with the dimensionless bedform length (R^2
 349 = 0.66) (Figure 9e).

350 The bedform height and length predictions for dunes based on Van Rijn (1984) and
 351 Venditti and Bradley (2022) are shown in Figure 9a-b. For the low-discharge runs, these
 352 predictions overestimate the measured bedform dimensions significantly. However, the rip-
 353 ple predictor of Soulsby et al. (2012) performs relatively well, with root-mean-square errors
 354 of 0.001 m for height and 0.02 m for length. The bedforms can therefore be classified as
 355 ripples. For the medium and high discharge runs, the Soulsby et al. (2012) equation for
 356 ripples underpredicts the bedform size significantly. These bedforms are therefore classified
 357 as dunes. The predictor of Van Rijn (1984) performs reasonably well for medium transport
 358 stages, but it mostly underpredicts bedform heights for high transport stages. The predic-
 359 tor of Venditti and Bradley (2022) slightly overpredicts bedform height, but the measured
 360 values are still within their margins of error. The bedform length predictor of Van Rijn
 361 (1984), which is purely based on water depth, does not capture the trend of increasing dune
 362 length with increasing transport stage. The predictor of Venditti and Bradley (2022) largely
 363 overestimates bedform length for medium transport stages, but performs better for the high
 364 transport stages by capturing the observed increase in length.

365 3.3 Hydraulic roughness

366 Hydraulic roughness, expressed as the depth-independent Manning's n and calculated
 367 via the Law of the Wall based on the velocity profiles (equation (12)), averaged 0.038.
 368 Manning's n increased with increasing leeside angle ($R^2 = 0.31$) and decreasing bedform
 369 length ($R^2 = 0.40$) (Figure 10c-d). The relation with leeside angle stands out (Figure 10c),
 370 since the ripples and dunes are both part of the linear correlation, whereas no relation
 371 between ripple length and roughness was observed. Generally, the roughness was larger
 372 during the experiments with fine silt (Figure 10) and the experiments with a rippled bed
 373 (on average 0.039). The larger roughness is likely to be related to the relatively high leeside
 374 angle of the bedforms observed in those experiments.

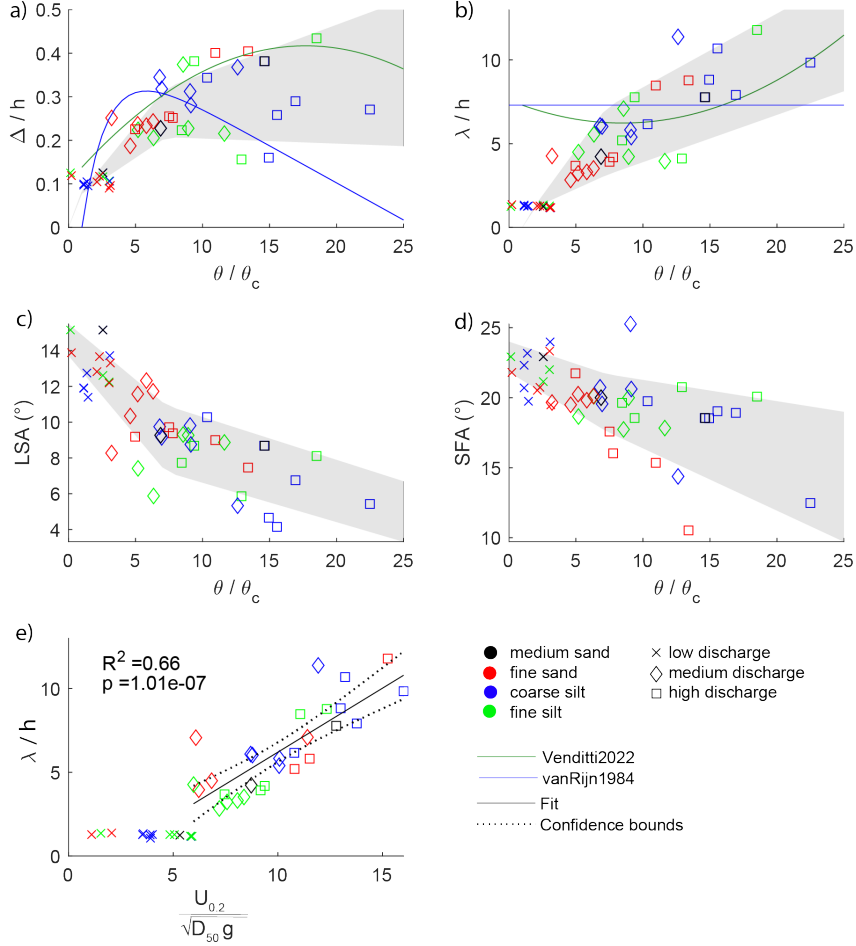


Figure 9. Increasing variability in bedform geometry with increasing flow strength, expressed as transport stage (θ/θ_c) in (a-d) and as non-dimensionalized velocity at 20% above the bed in (e). a) Bedform height divided by water depth. b) Bedform length divided by water depth. c) Leeward angle. d) Slip-face angle. e) Bedform length divided by water depth. Grey shading indicates one standard deviation from the mean value, in which the standard deviation is calculated from all bedforms in either low, medium or high discharge experiments. The base runs are indicated with black markers (medium sand). In (a) and (b), the predicted values by Venditti and Bradley (2022) and Van Rijn (1984) are shown.

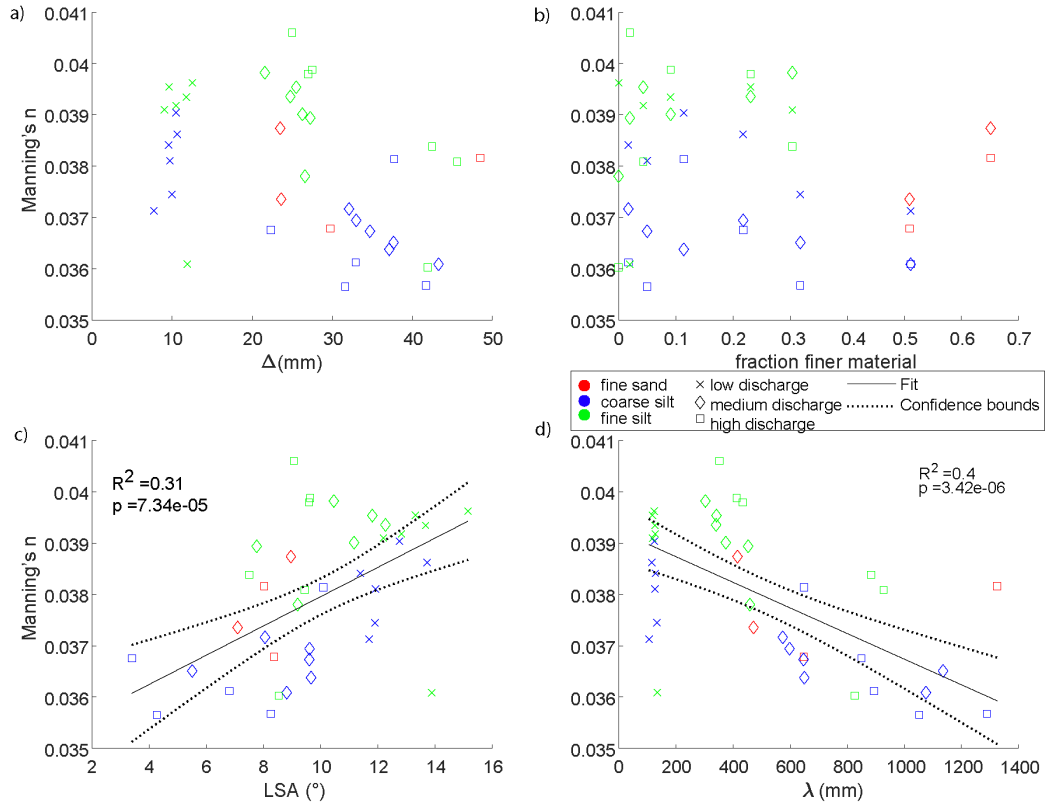


Figure 10. The relation between the hydraulic roughness n_{man} , calculated with the Law of the Wall, and a) Bedform height, Δ . b) Fraction finer material within the base material. c) Leaside angle, LSA . d) Bedform length, λ . Significant linear relations are shown in c and d.

Counter-intuitively, hydraulic roughness does not exhibit a statistically significant relationship with dune height and the fraction of added finer material (Figure 10a-b). The lack of a relationship with added fine material is consistent with the roughness predictor of Van Rijn (1984), which differentiates between skin friction, related to grain size, and form friction, related to bedform size. According to this predictor, on average, 97% of the total amount of friction is attributed to form friction in the experiments, indicating that bed composition is less important for hydraulic roughness than bedform geometry. The roughness predictor of Van Rijn (1984) yields on average a Manning's n of 0.030, which is 11% lower than the measured friction based on the Law of the Wall.

4 Discussion

4.1 A shift in transport stage due to addition of fines

The transport stage-based dune height predictor of Venditti and Bradley (2022) provides a way to visualize the experimental results and assess deviations from expected heights caused by the sediment mixtures (Figure 11). The predictor implies a parabolic relationship between bedform height and transport stage, as well as confidence levels for data variability (Bradley and Venditti, 2017). The parabolic relation can be interpreted as follows. As the transport stage increases, the transport mode changes from bed load to mixed load (w_s / u^* decreases), and dune height increases. This corresponds to our low and medium-discharge experiments. As the transport stage increases further, bedforms start to become washed-out, thus reducing the bedform height. This corresponds to our high-discharge experiments (Yalin, 1972; Naqshband et al., 2014).

Although this framework is generally associated with a change in flow strength (Shields number, θ), it can also be used to frame the experimental data using changes in sediment mobility (critical Shields number, θ_c) caused by the addition of fine material to a coarser base sediment (Figure 11). During the medium-discharge experiments, adding non-cohesive fine sand and coarse silt led to an increase in dune height and length. When comparing this to the expected change based on the predictor of Venditti and Bradley (2022) due to a decrease in D_{50} resulting from the addition of fine sediment, the change in bedform geometry was larger than expected. We attribute the increase in bedform size to an increase in mobility of the bed material (i.e. a decrease in θ_c), leading to a larger change in transport stage (Section 4.2) than expected based on the change in D_{50} (Supplementary Table S1). Therefore, adding fine, non-cohesive material leads to a shift to the right on the bedform height - transport stage diagram (Figure 11). In contrast, adding fine, weakly cohesive material to the bed decreases the mobility of the sediment (Section 4.3), and therefore decreases the transport stage, resulting in a decrease in bedform size, leading to a shift to the left on the diagram in Figure 11. Furthermore, the large variability in bedform geometry at the high transport stages is attributed to instabilities that occur when the system moves towards upper-stage plane bed (Section 4.4). Finally, the ripples formed at low discharge do not fit within the transport stage diagram, since ripple size is only dependent on grain size and not on flow velocity (Baas, 1994; Baas, 1999; Soulsby et al., 2012). Below, these changes are discussed in more detail.

4.2 Impact of non-cohesive fine sediment (sand and coarse silt)

4.2.1 Hiding-exposure effect

During the medium-discharge experiments, we observed an increase in dune size with larger fractions of fine non-cohesive material (fine sand and coarse silt) mixed into the base material. This may be attributed to an increased mobility of the coarse sediment. In mixed sediments, differently sized grains interact with the flow and with each other in a different way than in equally sized sediments (McCarron et al., 2019), leading to selective entertainment. This is called the hiding-exposure effect, where small grains are hidden

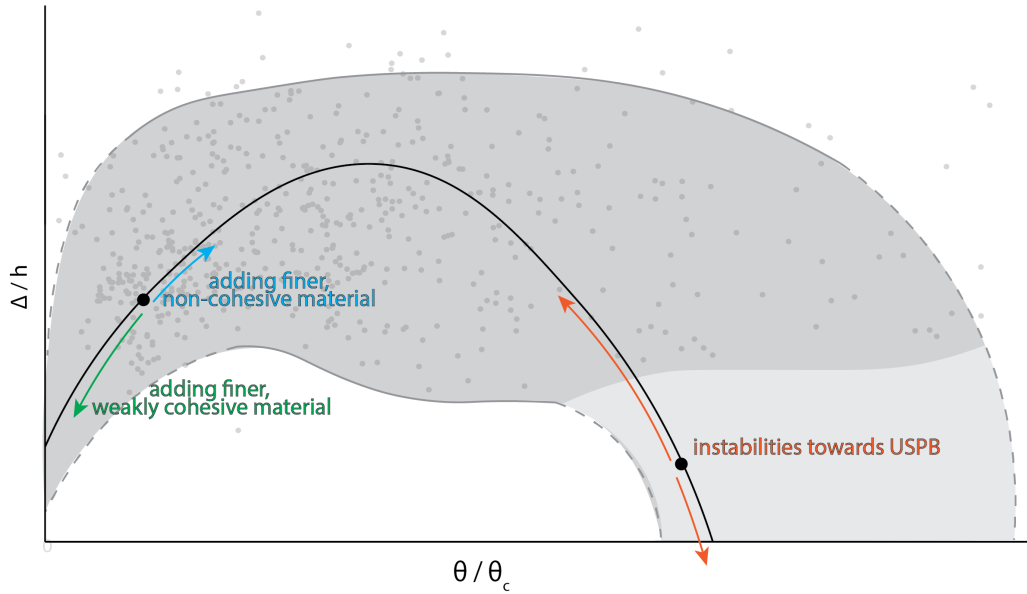


Figure 11. Conceptual diagram of non-dimensionalized dune height against transport stage, indicating the impact of adding non-cohesive and cohesive fine sediment to the bed material at relatively low transport stages, and the increased variability of bedform height due to flow instabilities at high transport stages. The dark grey shading indicates the 5 and 95-percentiles of data aggregated from Venditti et al. (2016) and Bradley and Venditti (2019). No data are available for the light grey shaded area. The dashed lines show the estimated course of the confidence intervals.

424 from the flow between the coarser grains. This does not only result in a more difficult
 425 mobilization of the fines (hiding), but also in an increased mobility of the larger grains
 426 (exposure) (Einstein, 1950) (see Section 4.2.2).

427 The hiding-exposure effect is mostly dependent on the ratio between the fraction of
 428 interest D_i (here, the coarse fraction) and the D_{50} . Hill et al. (2017) tested the influence of
 429 this ratio for gravel-sand mixtures. They found that if the two mixed sediments had similar
 430 grain sizes, ($D_{coarse} / D_{fines} < 2$), the bed aggregated without preferentially mobilizing the
 431 coarser fraction, and the fines became part of the bed structure (Frings et al., 2008). For
 432 intermediate particle ratios ($2 < D_{coarse} / D_{fines} < 20$), the fine sediment filled or bridged
 433 the pores of the coarser base matrix, resulting in increased mobility of the coarse fraction
 434 (Section 4.2.2). For large ratios ($D_{coarse} / D_{fines} > 20$), the fine sediment percolated
 435 through the base sediment. The subsurface became clogged, but the fines were not present
 436 in the surface layer, because all free fines were entrained and transported in suspension.

437 In the present experiments, the ratios between the coarse and fine fractions were 1.5,
 438 6.9 and 15 for fine sand, coarse silt and fine silt, respectively. Following Hill et al. (2017),
 439 this implies that the fine sand aggregated the bed structure, whereas the coarse and fine silt
 440 bridged or filled the pores of the coarse fraction. For the silts, the hiding-exposure effect
 441 should have played a role, increasing the mobility of the coarse fraction, whereas, for the fine
 442 sand, the increased size distribution might have resulted in increased mobility of the entire
 443 sediment bed due to an increase in grain protrusion and a decreased friction angle (Kirchner
 444 et al., 1990; Buffington et al., 1992). However, this effect may have been smaller than the
 445 mobility increase caused by the hiding-exposure effect by coarse silt, which is indicated by
 446 the increased lengthening of dunes in a bed with coarse silt compared to fine sand. Increased
 447 mobility means an increased transport stage, hence an increased dune length (Section 4.1).

448 Various methods have been developed to correct the initiation of motion of sediments
 449 for the hiding-exposure effect (see McCarron et al. (2019) for a review). Generally, the
 450 correction factor lowers the critical Shields number, θ_c , for the coarse fraction ($D_i > D_{50}$),
 451 and increases it for the fine fraction ($D_i < D_{50}$). The correction factor, ζ , commonly takes
 452 this form (Einstein, 1950; Wilcock, 1993):

$$\zeta = \alpha \left(\frac{D_i}{D_{50}} \right)^{-\beta} \quad (15)$$

453 where D_i is the grain size of the fraction of interest, β controls the strength of the
 454 hiding-exposure effect (Buffington and Montgomery, 1997; McCarron et al., 2019), and $\alpha =$
 455 1 for sediments with the same density. Exponent β has been approximated using σ_g , as a
 456 measure for sorting (Patel et al., 2013; McCarron et al., 2019): $\beta = 0.96$ for $\sigma_g < 2.85$ and
 457 $\beta = 2.67e^{-0.37\sigma_g}$ for $\sigma_g \geq 2.85$, where σ_g is determined with equation (4).

458 Applying this correction factor to the experimental data shows that adding a larger
 459 fraction of fine material results in a larger increase in mobility of the coarse material. For
 460 example, replacing 50% of the base material by fine sand causes θ_c of the base material to
 461 decrease from 0.021 to 0.019 (-11%) and to 0.016 for 50% coarse silt (-31%) (Supplementary
 462 Table S1). Applying this adjusted critical Shields number to our data reduces the root-
 463 mean-square error of the observed normalized dune height by 0.019 (-9%) and 0.032 (-15%)
 464 for fine sand and coarse silt, respectively, when evaluated against the predictor of Venditti
 465 and Bradley (2022). In contrast, the same adjustment increases the root-mean-square error
 466 for the experiments with fine silt by 0.011 (+6%) and causes the variability for the high
 467 discharge runs to remain high, with a root-mean-square error of 0.31. These results are
 468 discussed in Sections 4.3 and 4.4, respectively.

469 *4.2.2 The hiding-exposure effect in mixed gravel-sand and sand-silt beds*

470 The hiding-exposure effect is not commonly recognized in studies focused on sand-silt
 471 mixtures, and is mainly based on experiments in gravel-sand mixtures. McCarron et al.
 472 (2019) described an increase in mobility in gravel-sand experiments based on a decrease
 473 in θ_c by 64% compared to well-sorted sediment of a similar size (2.14 mm). Frings et al.
 474 (2008) speculated that hiding-exposure could result in a more mobile coarse fraction than
 475 a fine fraction in the downstream part of sand-bed rivers. Our observations with sand-silt
 476 mixtures show many parallels to gravel-sand mixtures, but on a smaller grain-size scale.
 477 We therefore infer from our experiments that the hiding-exposure effect also plays a role in
 478 sand-silt mixtures.

479 Mechanisms explaining the increased mobility of gravel in sand-gravel mixtures were
 480 suggested by Ikeda (1984) and subsequently built on in later studies (e.g. Li and Komar
 481 1986; Whiting et al. 1988; Dietrich et al. 1989; Wilcock 1993; Venditti et al. 2010). Firstly,
 482 by filling pores with fine grains, the pivoting angle of large grains is reduced, thus facilitating
 483 entrainment (Li and Komar, 1986). Secondly, there is a lower probability that particles in
 484 transport are caught in the wake of protruding particles and deposit, since particles protrude
 485 less far into the flow. Finally, filling pores with fine material results in a smoother bed, thus
 486 resulting in lower drag, which in turn increases the near-bed velocity. These suggestions were
 487 built upon by Venditti et al. (2010), who suggested that the infilling of the pores causes
 488 dampening of small wakes in the lee of particles, resulting in acceleration of the near-bed
 489 flow, which in turn mobilizes the larger particles. Our experimental results suggest that
 490 this acceleration of near-bed velocity is reflected in an increase in dune length and height
 491 at medium discharge (Figure 9d).

492 The observation that the sediment mobility increases when adding coarse silt to the
 493 bed is in line with what can be expected from experiments with gravel-sand mixtures, but
 494 opposes previous observations in laboratory experiments with sand-silt mixtures. Bartzke

et al. (2013) and Yao et al. (2022) observed that non-cohesive silt stabilizes the sediment bed, but at different concentrations ($\sim 1.4\%$ silt and $>35\%$, respectively), whereas, in our experiments, even at 50% coarse silt the mobility of the sediment was increased. Interestingly, Bartzke et al. (2013), whose experiments fall in the range of pore bridging ($D_{coarse} / D_{fines} = 5.5$), explained the filling of pore space as a reason for increased stability of the bed due to reduced hyporheic flow, rather than a reason for increased mobility of the coarse fraction as found in gravel-sand experiments (Section 4.2.1). The reason for these opposing effects could lie in the different experimental setups: the highest flow velocity tested in these experiments was 0.35 m s^{-1} , which is comparable to our lowest flow velocity. It is therefore likely that the supposed stabilizing effect of silt is overruled by a large bed shear stress and the development of bedforms in our experiments.

Ma et al. (2020) studied the mobility of silt-sized sediment and the effects of sorting in laboratories and rivers world-wide, and found a high-mobility sediment transport regime related to the size and sorting of the bed sediment. Bed sediments of $D_{50} < 88 \mu\text{m}$ and poorly sorted sediments within a range of $88 \mu\text{m} < D_{50} < 153 \mu\text{m}$ were found to be more mobile than expected from the sediment transport rate equations of Engelund and Hansen (1967), whereas sediments with $D_{50} > 153 \mu\text{m}$ confirmed these equations. In other words, poorly sorted sediments in the transitional range of very fine to fine sand are more easily mobilized than narrowly distributed sediments. This agrees with equation (15), where the strength of the hiding-exposure effect is related to the sorting of the material. Although Ma et al. (2020) did not explicitly mention the hiding-exposure effect, and related their observation to the change from mixed load to suspended-load dominated transport, the hiding-exposure effect may have played a role to achieve this change.

4.3 Impact of weakly cohesive fine silt

Contrary to the increase in mobility observed when adding non-cohesive fine material, the mixing of fine silt into the bed reduced both the height and length of the bedforms. This can be attributed to the weakly cohesive character of the $17 \mu\text{m}$ -sized silt, because cohesive sediments such as clay are known to limit or suppress bedform growth (Schindler et al., 2015; Parsons et al., 2016) through London-van der Waals forces and by interparticle electrostatic bonding (Mehta, 2014), consequently increasing θ_c .

The fine silt used in our experiments exhibited weakly cohesive properties, confirmed by visual stickiness of slurries of the fine silt and an increased angle of repose. Therefore, fine silt might have imparted similar attractive forces as clay, although to a lesser extent. Schindler et al. (2015) and Parsons et al. (2016) performed experiments with fine sand ($D_{50} = 239 \mu\text{m}$) at a mean velocity $u = 0.8 \text{ m s}^{-1}$, and observed an inverse linear relationship between dune height and clay percentage, with a lack of dunes at a clay percentage of 15%. The sharp decline in bedform height with clay content as observed in their experiments, was not evident in the present experiments, and the bed remained mobile up to 30% fine silt. Nevertheless, in the medium-discharge experiments, the dune heights and lengths for fine silt were significantly reduced, as opposed to the increase for coarse silt and fine sand, likely due to decreased mobility of the entire bed. In the low-discharge experiments, the ripple size was reduced too, but, as shown below, this could be a result of decreased grain size rather than decreased mobility.

Wu et al. (2022) recorded a decrease in ripple height with increasing clay percentage under wave-current conditions ($D_{coarse} / D_{fines} \sim 51$). Below 11% clay, the clay was winnowed out of the bed, allowing clean-sand ripples of similar size to develop. Above 11%, the cohesiveness of the bed was large enough to limit bed mobility, and only small ripples formed. In our experiments, this effect did not occur, as even at small percentages of fine silt ($\sim 2\%$) bedform height decreased, as in the current-ripple experiments with mixed clay-sand of Baas et al. (2013). During the medium-discharge experiments, cohesion impeded dune formation, and only small bedforms formed. In the high-discharge experiments,

546 dunes did form, but their planform was more similar to the dunes formed in the medium-
 547 discharge experiments with fine sand and coarse silt than to those in the high-discharge runs
 548 (Supplementary Figure S2 and S3), indicating cohesion-induced hampered mobility.

549 In summary, the formation of relatively small bedforms in our experiments with fine
 550 silt can be attributed to reduced mobility, caused by the weakly cohesive properties of fine
 551 silt. This effect is less pronounced than in previous experiments with more strongly cohesive
 552 clay, in which the mobility was limited more strongly. The decreased mobility leads to an
 553 increase in the critical Shields number, and a shift to the left in the transport-stage diagram
 554 of Figure 11.

555 **4.4 Instabilities at high discharges**

556 The present study shows that any impact of fine sediment on bed geometry at high
 557 transport stages is swamped by the inherent variability of dune geometry (Figure 11). This
 558 variability encompasses three bed configurations, without any apparent relationship with the
 559 type or fraction of fines: a dune-covered bed; a flat bed with one large dune (cf. Saunderson
 560 and Lockett (1983) and Naqshband et al. (2016)); and a completely flat bed.

561 The variability in bedform geometry and the presence of multiple bed configurations
 562 have been described before in literature. Saunderson and Lockett (1983) performed experi-
 563 ments around the transition from dunes to upper-stage plane bed and found four different
 564 bed states: asymmetrical dunes; convex dunes; humpback dunes (comparable to the single
 565 large dune configuration in this study); and a flat bed. These bedform states were seen to
 566 transform into one another. Saunderson and Lockett (1983) dedicated this behavior to the
 567 close position of the bed to the phase boundary between dunes and upper-stage plane bed,
 568 but did not provide a physical explanation. Venditti et al. (2016) observed three phases in
 569 high-velocity experiments: a plane bed with washed-out dunes; a field of large dunes; and
 570 a field of small dunes. The water depth, shear stresses and water surface slope co-varied
 571 with the changes in bed configuration. During the plane-bed phase, intense localized erosion
 572 was followed by the formation of small or large bedforms, which then washed out to form
 573 a new flat bed. These cycles lasted from several minutes to more than half an hour, with
 574 transitions between individual bedform types happening in seconds or minutes. Similarly,
 575 Bradley and Venditti (2019) stated a 'tremendous variability' between bed states at a high
 576 transport stage, and reasoned that numerous observations of the bed are needed to get an
 577 average bed state that scales with the transport states described by equations (8) and (9).

578 However, none of these studies provided an explanation for the large variability in dune
 579 height at high transport stages. de Lange et al. (2023) reanalyzed the data of Venditti et al.
 580 (2016) and Bradley and Venditti (2019), and found a bimodal dune height distribution at
 581 high transport stages. They attributed this to a critical transition, exhibiting flickering
 582 between a high and low alternative stable state. Our current observations support the idea
 583 of these alternative stable states. The large variability in bed configurations explains the
 584 lack of a predictable succession of bed states with increasing amounts of fine sediment in
 585 the current study. This variability is so large that all bed states can occur at any moment,
 586 independent of the bed composition. However, the upper stage plane bed condition was
 587 not observed in the high-discharge experiments with fine silt, which once again shows a
 588 decreased mobility as a result of the cohesiveness of the sediment, leading to a shift to the
 589 left on the bedform-transport stage diagram, preventing flattening of the bed.

590 **4.5 Ripples at low discharges**

591 Ripples formed in the low discharge experiments. Ripple height and length are a product
 592 of the size of the bed material, and are independent of flow velocity (Baas, 1994; Baas, 1999;
 593 Soulsby et al., 2012). Therefore, the transport stage framework as suggested above for dunes
 594 is not relevant for ripples. The height and width of the ripples, and to a lesser degree their

length, decreased with an increasing amount of coarse and fine silt. The decrease in height is most apparent at silt concentrations above 20%, the same percentage at which the D_{10} of the sediment distribution drops considerably (Figure 3).

Adding fine sand to the base material led to a decrease in height of about 15%, a similar decrease as expected based on Soulsby’s ripple predictor (equation (10)). This suggests that the change in grain size dominated the change in ripple height, and the hiding-exposure effect was small. However, adding coarse silt to the base material had a larger decreasing effect on height and length than fine sand. In the run with 50% coarse silt, both the height and the length were at, or close to the predicted values of 8 mm and 95 mm, respectively, suggesting that equilibrium was reached in this run. Hence, adding coarse silt increases the development rate of the ripples compared to fine sand. This may be caused by three processes; a) a mobility increase induced by the hiding-exposure effect; b) a shorter equilibrium time for coarse silt ripples at the same Shields stress; c) a larger relative effect of coarse silt than fine sand, as a 50% increase in weight of the finer fraction involves a much larger number of coarse silt than fine sand particles (in the same volume, there are 331 times more coarse silt particles than medium sand particles, as opposed to 3 times for fine sand). Finally, adding fine silt to the base material shows the effect of cohesion by reducing the ripple height. However, the effect of particle size cannot be distinguished with confidence from that of cohesion. The decrease in ripple height with increasing fraction of fine silt is larger than for coarse sand, which might be at least partly caused by the cohesive properties of the fine silt.

It should be emphasized that the response of ripples to an increase of fine bed sediment is different from the response of dunes. Whereas dune geometry gets adjusted by the increased mobility of the non-cohesive bed sediment, ripple geometry mainly results directly from the particle size distribution of the material.

4.6 The impact of bed sediment on hydraulic roughness

We confirm that for relatively steep dunes, roughness is related to the steepness of the leeside, consistent with findings of Kwoll et al. (2016) and Lefebvre and Winter (2016). At the leeside of the dune, flow separation generates turbulence, resulting in energy dissipation in the turbulent wake, which constitutes the main source of dune-related roughness (Lefebvre et al., 2014; Venditti and Bennett, 2000). In our experiments, the bedforms had on average a leeside angle of 10° with a relatively steep section (mean slip-face angle 20°), resulting in intermittent flow separation (Lefebvre and Cisneros, 2023). The presence of flow separation can also be determined using the defect Reynolds number (Baas and Best, 2000), Re_d ($Re_d = \frac{\Delta u^*}{\nu}$). In all our experiments, Re_d is far larger than 4.5, which indicates the presence of flow separation (Williams and Kemp, 1971; Best and Bridge, 1992; Gyr and Müller, 1996).

Previous research suggested that the composition of the sediment bed has only a small influence on hydraulic roughness (Smith and McLean, 1977). This corresponds with our findings and equation (13) as far as skin friction is concerned; only 3% of the total roughness is attributed to skin friction in the present experiments. However, the bed composition strongly impacts the bed geometry, thereby influencing form roughness.

4.7 Wider implications

Our results show that the presence of fines affects sediment mobility, even if the fines only slightly change the D_{50} of the sediment. Therewith, fine material influences bedform properties and hydraulic roughness, which is worth accounting for in bedform size predictors. Moreover, the interaction of fine silt and sand with coarser sand is relevant for channel nourishment aimed at preventing incision (Czapiga et al., 2022).

To adequately determine bedform geometry, some measure of bimodality or sorting may be included in future predictors. This measure could focus on the fine fraction, such as the D_{10} . Additionally, the bed geometries for added fine and coarse silt differ notably,

644 if the fine silt fraction is cohesive. Hence, assessing the cohesive properties of silt, such as
 645 yield stress and viscosity, is crucial, and lumping fines into one fraction, with a cut-off at 63
 646 μm (e.g. Rijn (2020)) is to be avoided.

647 5 Conclusions

648 We performed 52 laboratory experiments, in which the bed composition was varied
 649 using three different sediment mixtures (medium sand with fine sand, coarse silt and fine
 650 silt) in different ratios, for three different discharges (low, medium, high). We measured the
 651 bed morphology at the end of the experiments to assess the effect of bed composition on
 652 bedform geometry, and used this to indirectly assess sediment mobility and transport stage.
 653 The main conclusions of the research are:

- 654 • Bedform response to the addition of fine material depends, amongst others, on trans-
 655 port capacity, bimodality-impacted bed mobility, and cohesion.
- 656 • In the dune regime, adding fine sand or coarse silt to medium sand increases the
 657 mobility of coarser material. This leads to an increase in transport stage, θ/θ_c , an
 658 increase in dune length, and an increase or decrease in dune height, depending on the
 659 initial value of θ/θ_c .
- 660 • The increase in mobility of medium sand is inferred to be caused by the hiding-
 661 exposure effect, with the filling of pores by coarse silt leading to a larger near-bed
 662 flow velocity. Fine sand is too coarse to fit in the pores, which causes an increase in
 663 grain protrusion and a decrease in friction angle, and therefore increased sediment
 664 mobility.
- 665 • Adding weakly cohesive fine silt to medium sand has a similar effect to adding cohesive
 666 clay (Schindler et al., 2015), by causing a decrease in transport stage and inhibiting
 667 dune growth.
- 668 • In the ripple regime, adding fine material leads to a decrease in ripple height, which
 669 responds directly to the decreased particle size.
- 670 • In the transitional regime from dune to upper-stage plane bed, bed geometries may
 671 flicker between alternative stable bed states, complicating the relation between bed-
 672 form height and length and fine sediment fraction.
- 673 • The composition of the sediment bed does not significantly influence hydraulic rough-
 674 ness from skin friction drag, but it alters the bed morphology, and thus indirectly
 675 changes the hydraulic roughness through form drag.

676 Appendix A Bedform geometry predictors

677 The dune height and length predictions based on Van Rijn (1984) follow equation (6)
 678 and (7) in which T is Van Rijn (1984)'s definition of the transport stage.

$$T_{vRijn} = \frac{(u^*)^2 - (u_c^*)^2}{(u_c^*)^2} \quad (\text{A1})$$

679 where u^* is the shear velocity (m s^{-1}), and u_c^* is the critical shear velocity (m s^{-1}). Both the
 680 shear velocity and the critical shear velocity are unknown, but can be expressed in known
 681 parameters. The shear velocity can be expressed via:

$$u^* = u \frac{g^{0.5}}{C'} \quad (\text{A2})$$

682 in which u is the time and depth-averaged velocity (m s^{-1}) derived from the measurements
 683 with the UB-LAB 2C and C' is the grain-related Chézy parameter ($\text{m}^{0.5} \text{s}^{-1}$), which can
 684 be expressed as:

$$C' = 18 \log \frac{12R_h}{3D_{90}} \quad (\text{A3})$$

685 Herein, R_h is the hydraulic radius, which is equal to the cross-sectional area (A) divided by
 686 the wetted perimeter ($P = \text{width} + 2h$).

687 The critical shear velocity can be calculated as:

$$u_c^* = \sqrt{\frac{\tau_c}{\rho_w}} \quad (\text{A4})$$

688 In turn, the critical shear stress can be calculated using the critical Shields number θ_c :

$$\tau_c = \theta_c(\rho_s - \rho_w)gD_{50} \quad (\text{A5})$$

689 and θ_c is obtained from (Parker et al., 2003):

$$\theta_c = 0.5 \left(0.22Re_p^{-0.6} + 0.06 * 10^{(-7.7Re_p^{-0.6})} \right) \quad (\text{A6})$$

690 In which the particle Reynolds number, Re_p (-), is defined as:

$$Re_p = D_{50}^{3/2} \frac{\sqrt{\rho_r g}}{\nu} \quad (\text{A7})$$

691 Venditti and Bradley (2022)'s empirical equation for predicting dune height and length
 692 can be found in equation (8) and (9). The dimensionless shear stress θ is derived by calcula-
 693 ting the shear stress τ from the shear velocity (via equation (A4), replacing τ for τ_c). The
 694 critical shear stress θ_c is calculated via equation (A6).

695 The geometry of ripples is predicted based on Soulsby et al. (2012) via equation (10)
 696 and (11) in which D^* (-) is given by:

$$D^* = D_{50} \left(\frac{g(\frac{\rho_s}{\rho_w} - 1)}{\nu^2} \right)^{1/3} \quad (\text{A8})$$

697 **Appendix B Hydraulic roughness determination**

698 For a water column that satisfies equation (12), the equation can be rewritten into:

$$\bar{u}(\sigma_d) = \frac{u^*}{\kappa} (\ln(\sigma_d) + 1) + U \quad (\text{B1})$$

699 in which U is the depth-mean velocity, and σ_d is the dimensionless depth using:

$$\sigma_d = \frac{z + h}{h} \quad (\text{B2})$$

700 The value of u^* can be derived from the slope of a linear regression line through the
 701 data points of \bar{u} versus $(\ln(\sigma_d)+1)$. The average velocity $\bar{u}(\sigma_d)$ was determined as the
 702 average streamwise velocity during a single measurement. The averaging time window of
 703 30 minutes was narrowed down to cover an integer number of bedforms, defined from top
 704 to top. The σ_d -coordinate was defined such that $\sigma_d=0$ coincides with the top of the highest

705 bedform during a measurement (the 95-percentile of the measured bed elevation was chosen,
 706 to exclude outliers as a result of backscatter spikes). The $\sigma_d=1$ -coordinate is located at the
 707 top of the vertical measuring range, which corresponds to the elevation of the UB-Lab-2C
 708 transducer. The time-averaged relation between \bar{u} and $\ln(\sigma_d)$ was consistently linear at the
 709 middle half of the measured profile (between $-0.175 < \sigma_d < -0.625$), so this part of the
 710 profile was used for determining u^* (Supplementary Figure S6). The goodness of the linear
 711 fit of the log-profiles had on average a R^2 -value of 0.96. Following Hoitink et al. (2009), the
 712 roughness length z_0 (m) can be calculated using:

$$z_0 = \frac{h}{e^{\left(\frac{\pi U}{u^*}\right)} + 1} \quad (\text{B3})$$

713 Finally, Manning's n, n_{man} ($\text{s m}^{-1/3}$) can be calculated in the following steps (Pope,
 714 2000; Chow, 1959):

$$k_b = 30 * z_0 \quad (\text{B4})$$

$$n_{man} = \frac{k_b^{\frac{1}{6}}}{25} \quad (\text{B5})$$

715 in which k_b is the total roughness height (m).

716 Roughness height can also be approximated indirectly based on the predictor of Van
 717 Rijn (1984) with equation (13), resulting in the dimensionless Darcy-Weisbach friction fac-
 718 tor, \hat{f} . Herein, k_s consists of form roughness height k_{sf} and grain roughness height k_{sg} :

$$k_s = k_{sg} + k_{sf} \quad (\text{B6})$$

$$k_{sg} = 3D_{90} \quad (\text{B7})$$

$$k_{sf} = 1.1\gamma_d\Delta\left(1 - e^{-\frac{25\Delta}{\lambda}}\right) \quad (\text{B8})$$

719 where the calibration constant γ_d is taken as 1 in laboratory conditions (Van Rijn, 1984).

720 The friction factor, \hat{f} , can be converted to Manning's n (n_{man}) via the Chézy coefficient
 721 C ($\text{m}^{1/2}\text{s}^{-1}$) (Manning, 1891; Silberman et al., 1963).

$$C = \frac{R_h^{1/6}}{n_{man}} \quad (\text{B9})$$

$$\hat{f} = \frac{8g}{C^2} \quad (\text{B10})$$

722 Open Research Section

723 The data and code used to generate the results in this study will be made available
 724 through the public repository of 4TU upon acceptance, with doi: 10.4121/dde430c4-7f9f-
 725 4d7b-bff1-d4792e0031f2.

Acknowledgments

SdL and TH were funded by the Netherlands Organization for Scientific Research (NWO), within Vici project “Deltas out of shape: regime changes of sediment dynamics in tide-influenced deltas” (Grant NWO-TTW 17062). IN is funded by the Dutch Ministry of Infrastructure and Water under the research program “Rivers2Morrow”. This work is based on the MSc thesis of SV and JL. We would like to thank Maarten Kleinhans and Jeremy Venditti for their help with data interpretation, Nick Wallerstein for the technical and practical help in the laboratory, and finally all fellow colleagues that helped shovelling sediment in and out of the flume.

References

- Allen, J. R.L. (1978). “Computational models for dune time-lag: calculations using Stein’s rule for dune height”. In: *Sedimentary Geology* 20.C, pp. 165–216. ISSN: 00370738. DOI: 10.1016/0037-0738(78)90054-4.
- ASCE Task Force (2002). “Flow and transport over dunes”. In: *Journal of Hydraulic Engineering* 127, pp. 726–728.
- Baas, J.H. and H. de Koning (1995). “Washed-Out Ripples: Their Equilibrium Dimensions, Migration Rate, and Relation to Suspended-Sediment Concentration in Very Fine Sand”. In: *SEPM Journal of Sedimentary Research* Vol. 65A. ISSN: 1527-1404. DOI: 10.1306/D42680E5-2B26-11D7-8648000102C1865D.
- Baas, Jaco H. (1994). “A flume study on the development and equilibrium morphology of current ripples in very fine sand”. In: *Sedimentology* 41.2, pp. 185–209. ISSN: 13653091. DOI: 10.1111/j.1365-3091.1994.tb01400.x.
- (Feb. 1999). “An empirical model for the development and equilibrium morphology of current ripples in fine sand”. In: *Sedimentology* 46.1, pp. 123–138. ISSN: 00370746. DOI: 10.1046/j.1365-3091.1999.00206.x.
- Baas, Jaco H. and James L. Best (Aug. 2000). “Ripple formation induced by biogenic mounds—comment”. In: *Marine Geology* 168.1-4, pp. 145–151. ISSN: 00253227. DOI: 10.1016/S0025-3227(00)00040-2.
- Baas, Jaco H., Alan G. Davies, and Jonathan Malarkey (Jan. 2013). “Bedform development in mixed sand–mud: The contrasting role of cohesive forces in flow and bed”. In: *Geomorphology* 182, pp. 19–32. ISSN: 0169555X. DOI: 10.1016/j.geomorph.2012.10.025.
- Bartzke, Gerhard et al. (2013). “On the stabilizing influence of silt on sand beds”. In: *Journal of Sedimentary Research* 83.8, pp. 691–703. ISSN: 15271404. DOI: 10.2110/jsr.2013.57.
- Berg, J.H. van den and A. van Gelder (1993). “A new bedform stability diagram, with emphasis on the transition of ripples to plane bed in flows over fine sand and silt”. In: *Spec. Publs Int. Ass. Sediment* 17, pp. 11–21.
- Best, Jim (2005). “The fluid dynamics of river dunes: A review and some future research directions”. In: *Journal of Geophysical Research: Earth Surface* 110.4, pp. 1–21. ISSN: 21699011. DOI: 10.1029/2004JF000218.
- Best, Jim and John Bridge (1992). “The morphology and dynamics of low amplitude bed-waves upon upper stage plane beds and the preservation of planar laminae”. In: *Sedimentology* 39.5, pp. 737–752. ISSN: 13653091. DOI: 10.1111/j.1365-3091.1992.tb02150.x.
- Bradley, Ryan W. and Jeremy G. Venditti (Feb. 2017). *Reevaluating dune scaling relations*. DOI: 10.1016/j.earscirev.2016.11.004.
- (2019). “Transport Scaling of Dune Dimensions in Shallow Flows”. In: *Journal of Geophysical Research: Earth Surface* 124.2, pp. 526–547. ISSN: 21699011. DOI: 10.1029/2018JF004832.
- Buffington, John M., William E. Dietrich, and James W. Kirchner (Feb. 1992). “Friction angle measurements on a naturally formed gravel streambed: Implications for crit-

- 778 ical boundary shear stress”. In: *Water Resources Research* 28.2, pp. 411–425. ISSN:
779 00431397. DOI: 10.1029/91WR02529.
- 780 Buffington, John M. and David R. Montgomery (Aug. 1997). “A systematic analysis of eight
781 decades of incipient motion studies, with special reference to gravel-bedded rivers”.
782 In: *Water Resources Research* 33.8, pp. 1993–2029. ISSN: 00431397. DOI: 10.1029/
783 96WR03190.
- 784 Chow, V.T. (1959). *Open-channel hydraulics*. McGraw-Hill Book Company, USA. ISBN:
785 ISBN 0-07- 085906-X.
- 786 Czapiga, Matthew J., Astrid Blom, and Enrica Viparelli (June 2022). “Sediment Nourish-
787 ments to Mitigate Channel Bed Incision in Engineered Rivers”. In: *Journal of Hydraulic*
788 *Engineering* 148.6. ISSN: 0733-9429. DOI: 10.1061/(ASCE)HY.1943-7900.0001977.
- 789 Dade, W. Brian and Peter F. Friend (Nov. 1998). “Grain-Size, Sediment-Transport Regime,
790 and Channel Slope in Alluvial Rivers”. In: *The Journal of Geology* 106.6, pp. 661–676.
791 ISSN: 0022-1376. DOI: 10.1086/516052.
- 792 de Lange, S.I. et al. (Dec. 2023). “Alternative stable river bed states at high flow”. In: *ESS*
793 *Open Archive*. DOI: 10.22541/essoar.170317282.22054327/v1.
- 794 Dietrich, William E. (Dec. 1982). “Settling velocity of natural particles”. In: *Water Re-*
795 *sources Research* 18.6, pp. 1615–1626. ISSN: 00431397. DOI: 10.1029/WR018i006p01615.
- 796 Dietrich, William E. et al. (July 1989). “Sediment supply and the development of the coarse
797 surface layer in gravel-bedded rivers”. In: *Nature* 340.6230, pp. 215–217. ISSN: 0028-
798 0836. DOI: 10.1038/340215a0.
- 799 Einstein, H. A. (1950). “The bed-load function for sediment transportation in open chan-
800 nel flows”. In: *Technical Bulletins 156389, United States Department of Agriculture,*
801 *Economic Research Service*.
- 802 Englund, F. and E. Hansen (1967). “Monograph on Sediment Transport”. In: *Technisk*
803 *Forlag, Copenhagen, Denmark*.
- 804 Ferguson, R I and M Church (2004). *A simple universal equation for grain settling velocity*.
805 Tech. rep. 6, pp. 933–937. URL: [http://pubs.geoscienceworld.org/sepm/jshedres/
806 article-pdf/74/6/933/2821499/933.pdf](http://pubs.geoscienceworld.org/sepm/jshedres/article-pdf/74/6/933/2821499/933.pdf).
- 807 Frings, Roy M., Maarten G. Kleinhans, and Stefan Vollmer (Dec. 2008). “Discriminating
808 between pore-filling load and bed-structure load: A new porosity-based method, ex-
809 emplified for the river Rhine”. In: *Sedimentology* 55.6, pp. 1571–1593. ISSN: 13653091.
810 DOI: 10.1111/j.1365-3091.2008.00958.x.
- 811 Greene, H. Gary, Matthew Baker, and John Aschoff (2020). “A dynamic bedforms habitat
812 for the forage fish Pacific sand lance, San Juan Islands, WA, United States”. In: *Seafloor*
813 *Geomorphology as Benthic Habitat*. Elsevier, pp. 267–279. DOI: 10.1016/B978-0-12-
814 -814960-7.00014-2.
- 815 Gyr, A. and A. Müller (1996). “The role of coherent structures in developing bedforms
816 during sediment transport”. In: *Coherent flow structures in open channels*, pp. 227–
817 235.
- 818 Healy, T., Y. Wang, and J.A. Healy (2002). *Muddy Coasts of the World: Processes, Deposits*
819 *and Function*. 1st ed. Amsterdam: Elsevier.
- 820 Hill, Kimberly M. et al. (Jan. 2017). “Experimental study of the effect of grain sizes in a
821 bimodal mixture on bed slope, bed texture, and the transition to washload”. In: *Water*
822 *Resources Research* 53.1, pp. 923–941. ISSN: 19447973. DOI: 10.1002/2016WR019172.
- 823 Hoitink, A. J.F., F. A. Buschman, and B. Vermeulen (2009). “Continuous measurements of
824 discharge from a horizontal acoustic Doppler current profiler in a tidal river”. In: *Water*
825 *Resources Research* 45.11, pp. 1–13. ISSN: 00431397. DOI: 10.1029/2009WR007791.
- 826 Hurther, D. and U. Lemmin (2001). “A Correction Method for Turbulence Measurements
827 with a 3D Acoustic Doppler Velocity Profiler”. In: *Journal of Atmospheric and Oceanic*
828 *Technology*, pp. 446–458. DOI: [https://doi.org/10.1175/1520-0426\(2001\)
829 018<0446:ACMFTM>2.0.CO;2](https://doi.org/10.1175/1520-0426(2001)018<0446:ACMFTM>2.0.CO;2).
- 830 Ikeda, H. (1984). “Flume experiments on the superior mobility of sediment mixtures”. In:
831 *Ann. Rep. Inst. Geosci. 10*. Univ. of Tsukuba, Tsukuba, Japan, pp. 53–56.

- 832 Karim, F. (1995). “Bed configuration and hydraulic resistance in alluvial-channel flows”. In:
833 *Journal of Hydraulic Engineering* 121.1, pp. 15–25.
- 834 Kirchner, JAMES W. et al. (Aug. 1990). “The variability of critical shear stress, friction an-
835 gle, and grain protrusion in water-worked sediments”. In: *Sedimentology* 37.4, pp. 647–
836 672. ISSN: 0037-0746. DOI: 10.1111/j.1365-3091.1990.tb00627.x.
- 837 Kwoil, E. et al. (Mar. 2016). “Flow structure and resistance over subaqueous high- and
838 low-angle dunes”. In: *Journal of Geophysical Research: Earth Surface* 121.3, pp. 545–
839 564. ISSN: 21699011. DOI: <https://doi.org/10.1002/2015JF003637>.
- 840 Lefebvre, Alice and Julia Cisneros (July 2023). “The influence of dune lee side shape on
841 time-averaged velocities and turbulence”. In: *Earth Surface Dynamics* 11.4, pp. 575–
842 591. ISSN: 2196-632X. DOI: 10.5194/esurf-11-575-2023.
- 843 Lefebvre, Alice, Andries J. Paarlberg, and Christian Winter (Feb. 2014). “Flow separation
844 and shear stress over angle-of-repose bed forms: A numerical investigation”. In: *Water
845 Resources Research* 50.2, pp. 986–1005. ISSN: 00431397. DOI: 10.1002/2013WR014587.
- 846 Lefebvre, Alice and Christian Winter (2016). “Predicting bed form roughness: the influence
847 of lee side angle”. In: *Geo-Marine Letters* 36.2, pp. 121–133. ISSN: 14321157. DOI:
848 10.1007/s00367-016-0436-8.
- 849 Li, Zhenlin and D. Komar Paul (June 1986). “Laboratory measurements of pivoting angles
850 for applications to selective entrainment of gravel in a current”. In: *Sedimentology* 33.3,
851 pp. 413–423. ISSN: 0037-0746. DOI: 10.1111/j.1365-3091.1986.tb00545.x.
- 852 Ma, Hongbo et al. (2017). “The exceptional sediment load of fine-grained dispersal sys-
853 tems: Example of the Yellow River, China”. In: *Science Advances* 3.5, pp. 1–8. ISSN:
854 23752548. DOI: 10.1126/sciadv.1603114.
- 855 Ma, Hongbo et al. (2020). “Universal relation with regime transition for sediment transport
856 in fine-grained rivers”. In: *Proceedings of the National Academy of Sciences of the
857 United States of America* 117.1, pp. 171–176. ISSN: 10916490. DOI: 10.1073/pnas
858 .1911225116.
- 859 Manning, R. (1891). “On the flow of water in open channels and pipes”. In: *Transactions
860 of the Institution of Civil engineers of Ireland*.
- 861 Mark, C. F. van der and A. Blom (2007). *A new and widely applicable tool for determining
862 the geometric properties of bedforms*. Tech. rep. University of Twente.
- 863 McCarron, Connor J. et al. (Apr. 2019). “The hiding-exposure effect revisited: A method to
864 calculate the mobility of bimodal sediment mixtures”. In: *Marine Geology* 410, pp. 22–
865 31. ISSN: 00253227. DOI: 10.1016/j.margeo.2018.12.001.
- 866 Mehta, A.J. (2014). *An Introduction to Hydraulics of Fine Sediment Transport*. Ed. by N. J.
867 Hackensack. World Scientific.
- 868 Mignot, E., D. Hurther, and E. Bartelemy (Nov. 2009). “On the structure of shear stress and
869 turbulent kinetic energy flux across the roughness layer of a gravel-bed channel flow”.
870 In: *Journal of Fluid Mechanics* 638, pp. 423–452. ISSN: 0022-1120. DOI: 10.1017/
871 S0022112009990772.
- 872 Naqshband, S., J.S. Ribberink, and S.J.M.H. Hulscher (2014). “Using both free surface effect
873 and sediment transport mode parameters in defining the morphology of river dunes
874 and their evolution to upper stage plane beds”. In: *Journal of Hydraulic Engineering*
875 140.6, pp. 1–6. ISSN: 19437900. DOI: 10.1061/(ASCE)HY.1943-7900.0000873.
- 876 Naqshband, S. et al. (2016). “Modeling river dune development and dune transition to upper
877 stage plane bed”. In: *Earth Surface Processes and Landforms* 41.3, pp. 323–335. ISSN:
878 10969837. DOI: 10.1002/esp.3789.
- 879 Parker, Gary et al. (2003). “Effect of Floodwater Extraction on Mountain Stream Morphol-
880 ogy”. In: *Journal of Hydraulic Engineering* 129.11, pp. 885–895. ISSN: 0733-9429. DOI:
881 10.1061/(asce)0733-9429(2003)129:11(885).
- 882 Parsons, Daniel R. et al. (2016). “The role of biophysical cohesion on subaqueous bed form
883 size”. In: *Geophysical Research Letters* 43.4, pp. 1566–1573. ISSN: 19448007. DOI: 10
884 .1002/2016GL067667.
- 885 Patel, Shaileshkumar B, Prem Lal Patel, and Prakash Devidas (2013). *Threshold for initi-
886 ation of motion of unimodal and bimodal sediments*. Tech. rep. 1, pp. 24–33.

- 887 Perillo, Mauricio M., James L. Best, and Marcelo H. Garcia (2014). “A new phase diagram
888 for combined-flow bedforms”. In: *Journal of Sedimentary Research* 84.4, pp. 301–313.
889 ISSN: 15271404. DOI: 10.2110/jsr.2014.25.
- 890 Pope, Stephen B (2000). *Turbulent Flows*. Cambridge University Press.
- 891 Prokocki, Eric W. et al. (June 2022). “The morphology of fluvial-tidal dunes: Lower Columbia
892 River, Oregon/Washington, USA”. In: *Earth Surface Processes and Landforms* 47.8,
893 pp. 2079–2106. ISSN: 10969837. DOI: 10.1002/esp.5364.
- 894 Rijn, Leo C. van (Jan. 2020). “Erodibility of Mud–Sand Bed Mixtures”. In: *Journal of*
895 *Hydraulic Engineering* 146.1. ISSN: 0733-9429. DOI: 10.1061/(asce)hy.1943-7900
896 .0001677.
- 897 Ruijsscher, T.V. de et al. (2018). “Application of a Line Laser Scanner for Bed Form Tracking
898 in a Laboratory Flume”. In: *Water Resources Research* 54.3, pp. 2078–2094. ISSN:
899 19447973. DOI: 10.1002/2017WR021646.
- 900 Saunderson, Houston C and Francis P J Lockett (1983). “Flume experiments on bedforms
901 and structures at the dune-plane bed transition”. In: *Spec. Publ. int. Ass Sediment* 6,
902 pp. 49–58.
- 903 Schindler, Robert J. et al. (2015). “Sticky stuff: Redefining bedform prediction in modern
904 and ancient environments”. In: *Geology* 43.5, pp. 399–402. ISSN: 19432682. DOI: 10
905 .1130/G36262.1.
- 906 SICK (2012). *Ranger E/D reference manual – MultiScan 3D camera with Gigabit Ethernet*
907 *(E), 3D camera with Gigabit Ethernet (D)*. Tech. rep. Waldkirch, Germany: SICK
908 Sensor Intelligence.
- 909 Silberman, E. et al. (1963). “Friction factors in open channels”. In: *J. Hydraul. Eng.* 89.HY2,
910 pp. 97–143.
- 911 Smith, J. Dungan and S. R. McLean (Apr. 1977). “Spatially averaged flow over a wavy
912 surface”. In: *Journal of Geophysical Research* 82.12, pp. 1735–1746. ISSN: 01480227.
913 DOI: 10.1029/JC082i012p01735.
- 914 Soulsby, R. L., R. J.S. Whitehouse, and K. V. Marten (Apr. 2012). “Prediction of time-
915 evolving sand ripples in shelf seas”. In: *Continental Shelf Research* 38, pp. 47–62. ISSN:
916 02784343. DOI: 10.1016/j.csr.2012.02.016.
- 917 Southard, John B and Lawrence A Boguchwal (1990). “Bed configurations in steady unidi-
918 rectional water flows, part 2. Synthesis of flume data.” In: 60.5, pp. 658–679.
- 919 Van Rijn, L.C. (1984). “Sediment transport, part III: Bedforms”. In: *Journal of Hydraulic*
920 *Engineering* 110.12, pp. 1733–1754.
- 921 Venditti, J. G. et al. (July 2010). “Mobilization of coarse surface layers in gravel-bedded
922 rivers by finer gravel bed load”. In: *Water Resources Research* 46.7. ISSN: 19447973.
923 DOI: 10.1029/2009WR008329.
- 924 Venditti, Jeremy G. and Sean J. Bennett (Sept. 2000). “Spectral analysis of turbulent
925 flow and suspended sediment transport over fixed dunes”. In: *Journal of Geophys-*
926 *ical Research: Oceans* 105.C9, pp. 22035–22047. ISSN: 0148-0227. DOI: 10.1029/
927 2000JC900094.
- 928 Venditti, Jeremy G. and Ryan W. Bradley (Jan. 2022). “Bedforms in Sand Bed Rivers”.
929 In: *Treatise on Geomorphology*. Elsevier, pp. 222–254. ISBN: 9780128182352. DOI: 10
930 .1016/B978-0-12-409548-9.12519-9.
- 931 Venditti, Jeremy G., C. Y. Martin Lin, and Moslem Kazemi (June 2016). “Variability in
932 bedform morphology and kinematics with transport stage”. In: *Sedimentology* 63.4,
933 pp. 1017–1040. ISSN: 13653091. DOI: 10.1111/sed.12247.
- 934 Warmink, J. J. et al. (2013). “Quantification of uncertainty in design water levels due to
935 uncertain bed form roughness in the Dutch river Waal”. In: *Hydrological Processes*
936 27.11, pp. 1646–1663. ISSN: 08856087. DOI: 10.1002/hyp.9319.
- 937 Whiting, P.J. et al. (1988). “Bedload sheets in heterogeneous sediment”. In: *Geology* 16.2,
938 pp. 105–108. DOI: [https://doi.org/10.1130/0091-7613\(1988\)016%3C0105:
939 BSIHS%3E2.3.CO;2](https://doi.org/10.1130/0091-7613(1988)016%3C0105:BSIHS%3E2.3.CO;2).

- 940 Wilcock, Peter R. (Apr. 1993). “Critical Shear Stress of Natural Sediments”. In: *Journal*
941 *of Hydraulic Engineering* 119.4, pp. 491–505. ISSN: 0733-9429. DOI: 10.1061/(ASCE)
942 0733-9429(1993)119:4(491).
- 943 Williams, Philip B. and Patrick H. Kemp (Apr. 1971). “Initiation of Ripples on Flat Sedi-
944 ment Beds”. In: *Journal of the Hydraulics Division* 97.4, pp. 505–522. ISSN: 0044-796X.
945 DOI: 10.1061/JYCEAJ.0002932.
- 946 Wolanski, Eric (2007). *Estuarine Ecohydrology*. Elsevier Science. ISBN: 9780444530660. DOI:
947 10.1016/B978-0-444-53066-0.X5001-6.
- 948 Wu, Yongsheng et al. (2022). “Tidal propagation in the Lower Fraser River, British Columbia,
949 Canada”. In: *Estuarine, Coastal and Shelf Science* 264. November 2021, p. 107695. ISSN:
950 02727714. DOI: 10.1016/j.ecss.2021.107695. URL: [https://doi.org/10.1016/j](https://doi.org/10.1016/j.ecss.2021.107695)
951 [.ecss.2021.107695](https://doi.org/10.1016/j.ecss.2021.107695).
- 952 Yalin, M.S. (1964). “Geometrical Properties of Sand Wave”. In: *Journal of Hydraulic Engi-*
953 *neering* 90, pp. 105–119.
- 954 — (1972). *Mechanics of Sediment Transport*. Oxford: Pergamon Press.
- 955 Yao, Peng et al. (Sept. 2022). “Erosion Behavior of Sand-Silt Mixtures: Revisiting the Ero-
- 956 sion Threshold”. In: *Water Resources Research* 58.9. ISSN: 19447973. DOI: 10.1029/
957 2021WR031788.